



High-resolution stratigraphy and multiple luminescence dating techniques to reveal the paleoseismic history of the central Dead Sea fault (Yammouneh fault, Lebanon)



Maryline Le Béon^{a,*}, Ya-Chu Tseng^a, Yann Klinger^b, Ata Elias^c, Alexander Kunz^d, Alexandre Sursock^e, Mathieu Daëron^f, Paul Tapponnier^g, Rachid Jomaa^e

^a Department of Earth Sciences, National Central University, Taiwan

^b Institut de Physique du Globe de Paris, CNRS, France

^c Lebanese University, Faculty of Engineering 1, Tripoli, Lebanon

^d Department of Geosciences, National Taiwan University, Taiwan

^e National Council for Scientific Research, Lebanon

^f Laboratoire des Sciences du Climat et de l'Environnement, France

^g Earth Observatory of Singapore, Nanyang Technology University, Singapore

ARTICLE INFO

Keywords:

Dead Sea (Levant) fault
Paleoseismology
Luminescence dating OSL
pIRIR₂₂₅

ABSTRACT

Continuous sedimentation and detailed stratigraphy are key parameters for a complete paleo-earthquake record. Here, we present a new paleoseismological study across the main strike-slip fault branch of the Dead Sea fault in Lebanon. We aim to expand the current knowledge on local paleoseismicity and seismic behavior of strike-slip plate boundary faults and to explore the limitations of paleoseismology and dating methods. The trench, dug in the Jbab el-Homr basin, reveals a succession of remarkable, very thin (0.1 to 5 cm) palustrine and lacustrine layers, ruptured by at least 17 earthquakes. Absolute ages of 4 samples are obtained from three luminescence-dating techniques targeting fine-grain minerals. Blue-green stimulated luminescence (BGSL) on quartz and post-infrared infrared-stimulated luminescence at 225 °C on polymineral aliquots led to consistent ages, while ages from infrared-stimulated luminescence at 50 °C on polymineral aliquots appeared underestimated. The quartz BGSL ages are 26.9 ± 2.3 ka at 0.50 m depth and 30.8 ± 2.9 ka at 3.65 m depth. During this time period of 3.9 ka ([0; 9.1 ka]), 14 surface-rupturing events occurred with a mean return time of 280 years ([0; 650 years]) and probable clustering. This return time is much shorter than the 1127 ± 135 years return time previously determined at the Yammouneh site, located 30 km south. Although fault segmentation and temporal variations in the earthquake cycle remain possible causes for such different records, we argue that the high-resolution stratigraphy in Jbab is the main factor, enabling us to record small deformations related to smaller-magnitude events that may have been missed in the rougher strata of Yammouneh. Indeed, focusing only on larger events of Jbab, we obtain a mean return time of 720 years ([0; 1670 years]) that is compatible with the Yammouneh record.

1. Introduction

Paleoseismological trenches consist in excavating past surface ruptures that were preserved thanks to burial under more recent sediments (e.g., Sieh, 1978; McCalpin, 2009). Hence, continuous sedimentation and thin-layered stratigraphy from a low energy environment are key parameters for a complete and detailed paleo-earthquake record. The timing of a paleo-earthquake is bracketed by dating the youngest ruptured layer and the first layer deposited continuously on top of it. Once a complete earthquake chronology is established, the return time in-

between the events can be estimated, as well as the likelihood of an event in the future. Ground-rupturing events are usually considered to be $M > 6.5$ events (e.g. McCalpin, 2009), although evidence was found for the preservation of ruptures associated to smaller events in paleoseismic trenches (e.g. Streig et al., 2014; Liu-Zeng et al., 2015). Thus, most paleoseismological records certainly include events of various magnitudes, which limits the significance of recurrence intervals simply calculated from a number of events over a time interval (e.g. Akçiz et al., 2010; Liu-Zeng et al., 2015).

This study documents a paleo-earthquake record from the left-

* Corresponding author.

E-mail address: mlebeon@gmail.com (M. Le Béon).

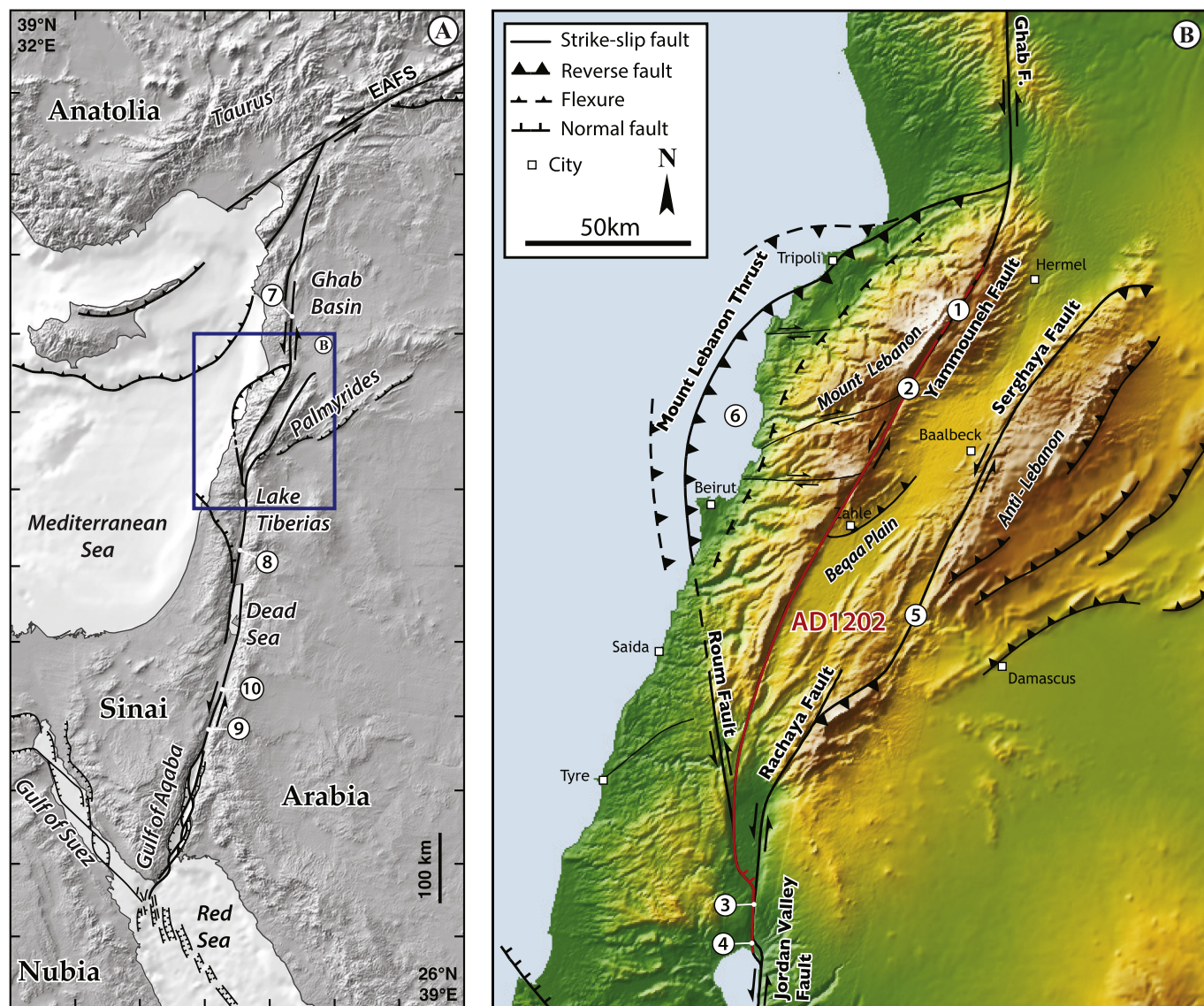


Fig. 1. a. Tectonic map of the Dead Sea fault system, the left-lateral plate boundary between Arabia and Sinai. Blue rectangle shows location of panel b. b. Tectonic map of the Lebanese Restraining Bend. The ground surface rupture of the AD1202 earthquake is shown in red. Numbers 1 to 10 show locations of paleo-seismological studies: 1: This study, Jbab el-Homr site; 2: Daëron et al. (2005, 2007), Yammounneh basin; 3: Ellenblum et al. (1998, 2015), Ateret fortress; 4: Wechsler et al. (2014, 2018); 5: Gomez et al. (2003); 6: Elias et al. (2007); 7: Meghraoui et al. (2003); 8: Ferry et al. (2011); 9: Klinger et al. (2015); Lefevre et al. (2018). (For interpretation of the references to color in this figure legend, the reader is referred to the web version of this article.) Maps are modified from Daëron et al. [2004].

lateral Dead Sea fault, a major plate boundary that accommodates the northward movement of the Arabia Plate relative to the Sinai sub-plate (Fig. 1a). This 1000-km-long fault system mainly strikes N0–10°E. However, in Lebanon, the main fault veers eastwards (N30°E), forming a 160-km-long restraining bend responsible for the uplift of Mount Lebanon (3088 m) (e.g. Dubertret, 1932; Quennell, 1959; Freund et al., 1968; Garfunkel et al., 1981). Transpression is partitioned between the offshore Mount Lebanon Thrust and two strike-slip faults, the Yamnourneh fault and the Serghaya-Rachaya fault (Gomez et al., 2003; Daëron et al., 2004; Elias et al., 2007; Goren et al., 2015) (Fig. 1b). The Yamnourneh fault was identified as the main strike-slip fault branch, with a Late Pleistocene slip rate of 5.1 ± 1.3 mm/a based on 25-ka-old offset alluvial fans dated by ^{36}Cl cosmogenic isotope (Daëron et al., 2004), while the Serghaya-Rachaya fault slip rate was determined to 1.4 ± 0.2 mm/a during the Holocene based on offset buried channels dated by radiocarbon (Gomez et al., 2003).

Historical testimonies attest to numerous devastating earthquakes

associated with local active faults during the last two millennia (e.g. Poirier and Taher, 1980; Ben-Menahem, 1991; Ambraseys et al., 1994; Guidoboni et al., 2004; Ambraseys, 2009). Paleoseismological studies aim at identifying the source of these events and at estimating earthquake recurrence intervals on individual faults, with the chief goals of understanding how earthquakes relate to each other in time and space and of improving seismic hazard assessment. Thanks to numerous paleoseismological studies in this region during the last two decades, several historical events could be located: the AD1202 event along the Yamnourneh fault (Daëron et al., 2005), the AD551 event along the Mount Lebanon Thrust (Elias et al., 2007), the AD1759 events pair along the Serghaya-Rachaya fault (Gomez et al., 2003), and the AD1837 event, which most likely occurred along the Roum fault (Nemer and Meghraoui, 2006) (Fig. 1b). Specific attention was given to the AD1202 event that testimonies describe as particularly devastating. Surface ruptures associated to this event were found from the northern shore of the Lake Tiberias and in the Jordan Gorge (Wechsler et al.,

2014, 2018; Ellenblum et al., 1998, 2015) to the Yammouneh basin (Daëron et al., 2005), making it a > 150-km-long ground surface rupture (Fig. 1b). While the AD1202 rupture was likely stopped in the south by a possible fault jog at the Lake Tiberias, the lack of significant earthquake barrier inferred from the fault trace morphology north of the Yammouneh basin suggests that it could have extended further north. Going further back in time, paleoseismic trenches in the Yammouneh basin have shown that the fault produced ground-rupturing earthquakes with a recurrence interval of 1127 ± 135 years during the Holocene (Daëron et al., 2007).

In order to extend the paleo-earthquake history in Lebanon and surroundings, this study investigates the paleo-earthquake record from a trench dug across the Yammouneh fault, 30 km north of the Yammouneh site (Daëron et al., 2007), at a site called Jbab el-Homr (Fig. 1b). In a first step, evidence of past ground surface ruptures in Jbab are described. Then, we present results from optically stimulated luminescence (OSL) dating that constrain the paleo-earthquake history. Next, we discuss these ages together with local paleoclimate proxies and interpret the evolution of the sedimentary environment. Finally, we analyze the earthquake chronology in Jbab, compare it with the Yammouneh site record, and discuss the implications for the seismic behavior of the Yammouneh fault and the effect of stratigraphic resolution on the interpretation of paleoseismological records.

2. Evidence for paleo-earthquakes in Jbab el-Homr

2.1. Setting of the trench site

The Yammouneh fault trace is located within the steep eastern flank of the Mount Lebanon range (Fig. 1b). The origin of the Jbab el-Homr basin, located at 1820 m above sea level, may be related to a change in the fault strike, from N40°E in the south to N20°E in the north (Fig. 2a). The geology around Jbab el-Homr consists in Cenomanian limestone. Several wadis (i.e. ephemeral stream in Arabic) feed the basin and deposited conglomerates at the basin edges (Daëron, 2005) (Fig. 2a). The conglomerate bedding dips show evidence of fault-parallel folding, probably associated with transpression along the N40°E section of the fault. A cumulative fault scarp, locally incised by channels that deposited inset alluvial fans (Figs. 2a, 3a), attest for a significant vertical component. The fans and channels also show evidence for left-lateral displacement. The cumulative scarp vanishes as the fault trends N20°E within the lowest part of the basin. There, the basin is flat, suggesting that it used to be a lake or a marsh. Nowadays, it is occasionally flooded by karstic springs (Figs. 2b, 3b) and it is covered in snow in winter. The fault trace is underlined by subtle micro-topography and changes in the soil color (Figs. 2b, 3b). The easternmost fault branch is quite obvious on satellite images from different dates available in the Google Earth database. Images acquired when the basin was partly flooded reveal an additional lineament located to the west of the excavated fault and that could correspond to another fault strand (Fig. 2b).

2.2. Overview of tectonic structures and stratigraphy

A first trench was excavated in 2003 within the lowest part of the basin, perpendicular to the fault (Figs. 2, 3, 4, Fig. S1), and investigated in detail for paleo-earthquakes. The trench was ~35 m long and 2.5 to 4 m deep. A second trench was excavated in 2009, ~15 m south of the 2003 trench (Fig. 2b), mainly for the purpose of collecting samples for OSL dating. Similar tectonic structures were found in both trenches. From meter mark 15 (MM15) to MM22, the main fault zone is characterized by a negative flower structure with a down-dropped block and intense deformation at MM17 (Fig. 4 and Fig. S1 of the 2003 trench). A secondary fault zone is found 12 m further east, at MM34. West of the main fault zone, between MM15 and MM4 (Fig. S1), only isolated fractures associated with minor deformation are observed.

Both trenches revealed a similar stratigraphic sequence, a

succession of thin layers (~1–5 cm thick), dominated by clay and silt, capped by a poorly developed plowed soil. Most layers can be followed across the trenches and can be correlated from one trench to the other. The lateral continuity of the layers and the grain size support the idea that a shallow lake or a marsh could have occupied the basin in the past. Orange-color horizons (1–10 cm thick) are occasionally superimposed to the layers and may represent episodes of dryer conditions when the soft sediments were exposed to the atmosphere and oxidized. From ~2.4 to ~1.5 m depth (at MM12), between layers 34 and 22, a distinctive sequence of very thin layers, 1 mm to 1 cm thick, alternately beige and dark brown, resembles seasonal varves (Fig. 3d, e, f, Fig. S1). Varve counting led to 125 pairs of light and dark layers, which would represent as many years if the varves were seasonal. Slightly thicker layers with different characteristics sometimes interrupt the varve sequence.

Layer correlation from MM22 to MM32 (Fig. 4) could be performed confidently above layer 30, simply following the layers along the trench wall. Beneath layer 30, the wall could not be completely cleaned and the layers appearance varies laterally, making correlation uncertain. We used specific labels for these layers of the eastern fault zone (MM32–35). In a tentative correlation, we simply extrapolate the strata horizontally, as generally observed in the trench. Then, layers Z34 and Z38 would correspond to layers 34 and 38, respectively.

2.3. Evidence for paleo-earthquakes

Past ground surface ruptures are recognized on the basis of sets of cracks, generally associated with 1–10 cm vertical offsets and that stop at a similar stratigraphic horizon. Vertical offsets may be related to oblique slip, to local transpressional or transtensional jogs along the rupture, or they may be apparent, due to changes in layer thickness, that are probably limited at this site. The thin layers exposed in the Jbab trench allowed for high-resolution recording of successive paleo-earthquakes, enabling us to distinguish crack terminations that are separated by few-centimeter-thick strata (Fig. 4, Fig. S1).

At least 17 earthquakes (labeled E1 to E17) were identified in the trench based on pieces of evidence highlighted in Fig. 4 and Fig. S1 and synthesized in Table 1. The total number of events is a minimum because the most recent faults reach the plowed soil, meaning that we cannot constrain if these faults correspond to one or several events. The events are associated with deformation of variable intensity and amplitude (Figs. 4 and 5, Fig. S1), which was used to classify them as locally small to very large events, with “small” corresponding to a lower-magnitude event or to decreasing slip at the rupture tip of a larger event. Events E5, E8 and E12 are characterized by a few faults with limited offsets and are classified as small events. Events E3, E4, E7, E10, and possibly E16 produced more numerous faults, across the whole trench, but still with limited offsets, and are classified as medium events. Events E6, E9, E11, E13, and E17 produced numerous faults, associated with vertical offsets in the order of 10 cm and are classified as large events. Some uncertainties remain on the exact timing of some of the significant offsets, as discussed in the next paragraph, leading to uncertainties on the size of some of the events. E1 could be large to very large, E2 could be nonexistent to large, E14 could be medium to very large and E15 small to very large. Overall, about half of all events were considered to be large, associated with ≥ 10 cm vertical offset.

We discuss here some of the uncertainties regarding the paleoseismological evidence (Table 1). Infrequent offsets larger than 10 cm are observed in the trench, but they could be associated to one or several events. Event E1 generated the largest vertical offset, with the ~50 cm down-drop of the central block D at MM17 (Fig. 5a). On the pre-E6 restoration (Fig. 5b), a significant vertical offset of ~30 cm remains between block A and block C for layer 38 and deeper, which may correspond to event E14 and/or E15. This raises two hypotheses: either infrequent events, such as E1 and E14 or E15, generate larger deformation, or this larger deformation actually results from several

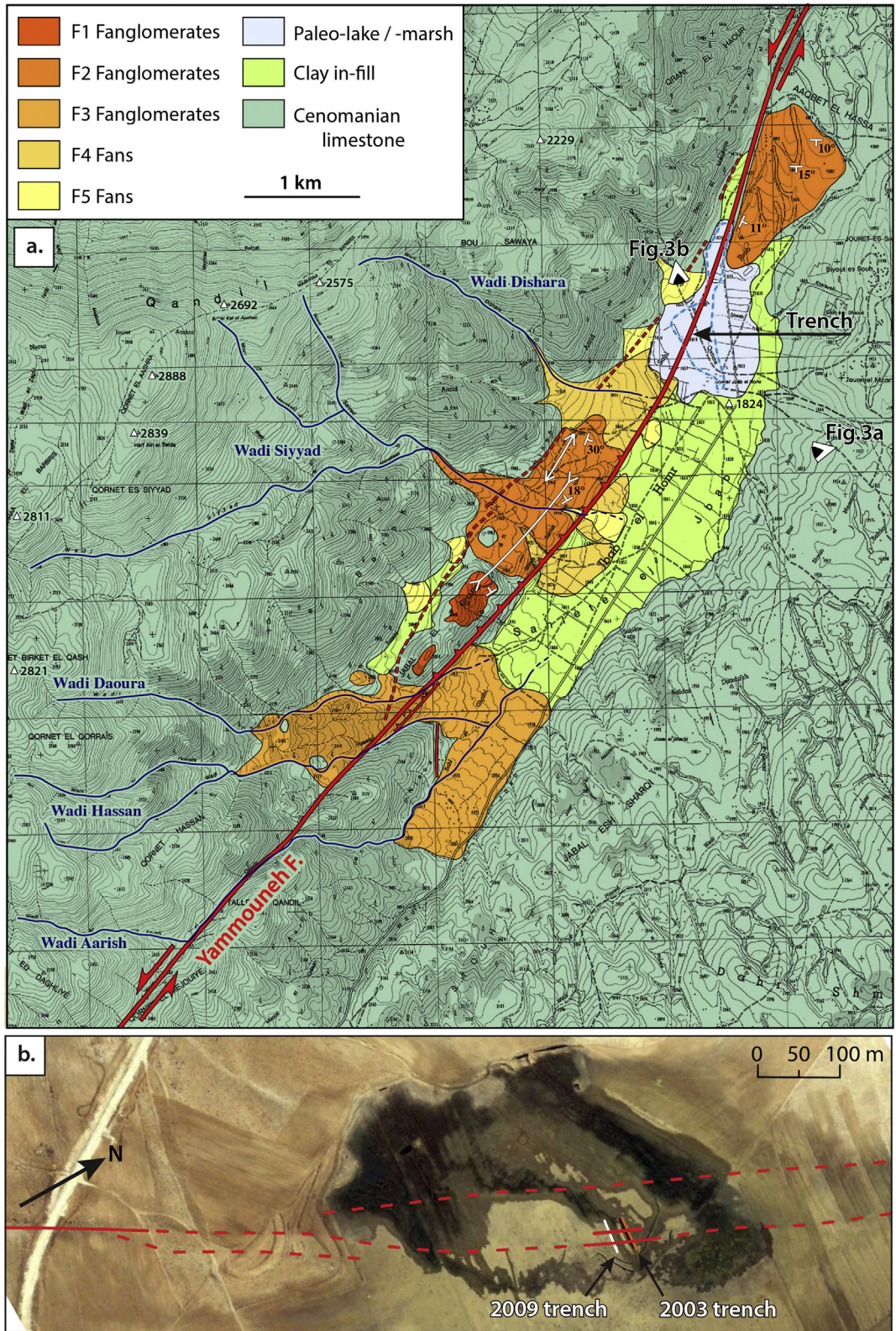
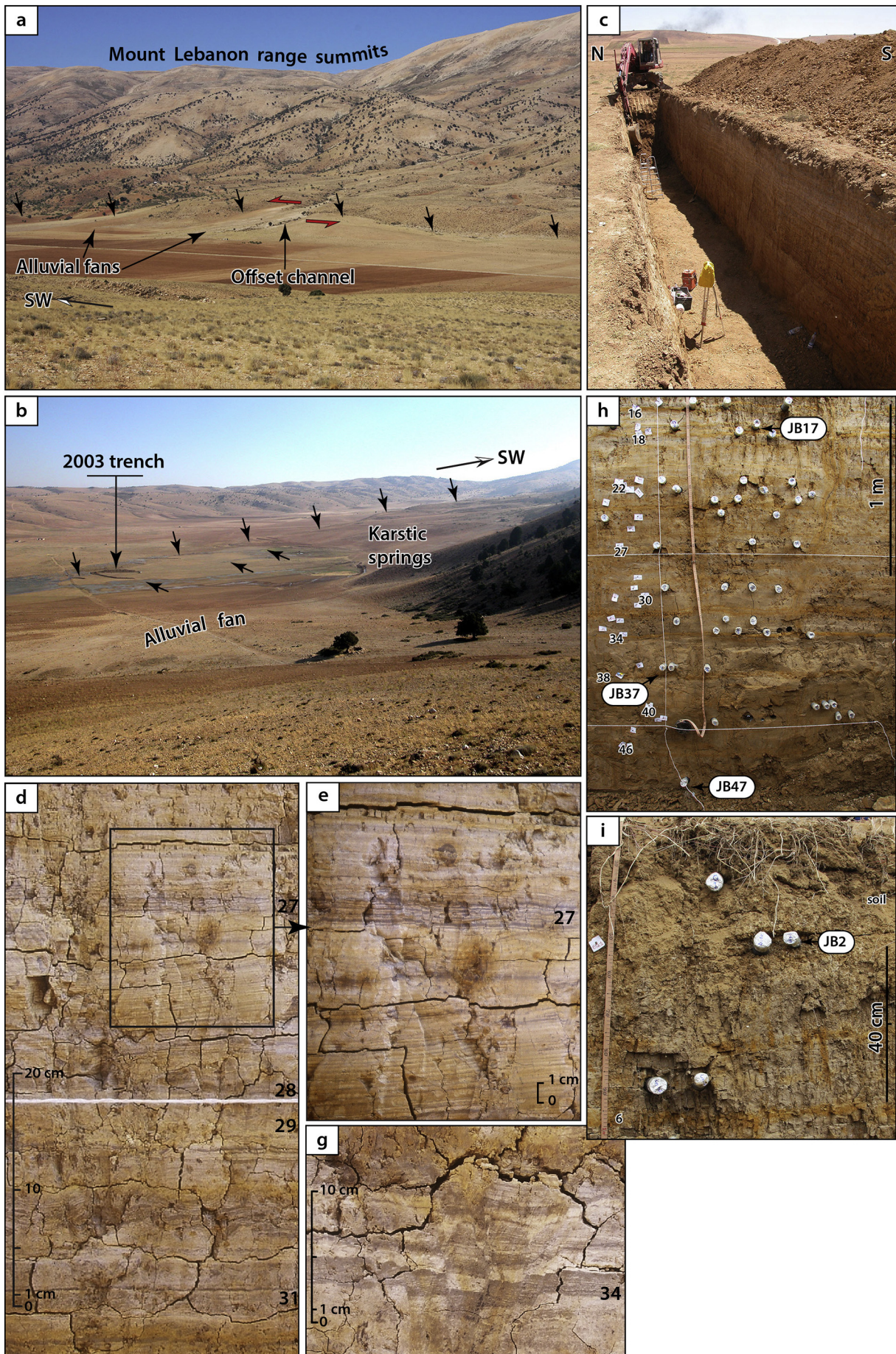


Fig. 2. a. Geological and morpho-tectonic map of the Jbab el-Homr area (modified from Daëron (2005)). Topographic map (scale 1:20,000, Direction des Affaires Géographiques, Beirut, Lebanon) is used as background. The blue dashed line and light-blue color fill show the extent of a 2-m and 12-m deep lake, respectively, sketched based on topographic contour lines. b. High-resolution satellite image of the basin, partly flooded (GoogleEarth, 10/23/2005 image). Red lines highlight fault-related lineaments. Continuous lines are faults evidenced from trenches or lateral geomorphic offsets visible. Dashed lines are inferred from lineaments on the images. (For interpretation of the references to color in this figure legend, the reader is referred to the web version of this article.)



(caption on next page)

Fig. 3. Field photographs of the Jbab el-Homr site, trench, and OSL samples. a. Overview of the cumulative fault scarp, incised gullies and channels, and inset fans along the N40°E section of the fault in the southern part of the Jbab el-Homr basin (Fig. 2). Black arrows point the fault. The bushes aligned along one of the wadis highlight a left-lateral offset of the channel. b. Overview of the lowest part of the basin in August 2003. Black arrows point the fault branches. c. Overview of the 2003 trench. d. Photograph of the varves section of the stratigraphy at MM13, away from faults. e. Detailed view of the varves. f. Detailed view of layer 34 deformed by a flower structure at MM6. g. and h. OSL sampling using 3.5 cm diameter PVC tubes in the 2009 trench. Arrows point the 4 samples dated in this study (JB2, JB17, JB37, JB47). Numbers indicate layers as in the trench logs (Fig. 4 and Fig. S1).

events in the case of E1 and from two events in the case of E14 and E15. Considering that one event out of two generates ~10 cm vertical offset, the ~50 cm down-drop associated to E1 could represent ~10 events.

Several faults and cracks reach the plowed soil along the trench. Because the youngest layers deposited within the main fault zone are absent laterally along the trench, some of these faults cannot be confidently associated to a specific event. For example, the faults at MM20 and MM22 affect layer 6 and could correspond to both E1 and E2, and the faults at MM35 that break layer 14a could correspond to any event from E1 to E4 or to several of them.

Event E2 is lightly constrained by a fault at MM17 that breaks and slightly offsets layers c4 and c3 (Fig. 4, Fig. S1). This fault is capped by layer c2 and has no clear downward termination. While we could argue for more potential evidence for E2 among the cracks that reach the plowed soil, we cannot rule out that the single fault at MM17 could correspond to the dying-out tip of a fracture plane related to a more recent event (Bonilla and Lienkaemper, 1990).

Beneath layer 18, the central part of the main fault zone (MM17) has been difficult to map and interpret due to intense deformation and difficulties in layer correlation. Yet, it seems unlikely that events were missed, because all events (except E2) are supported by faults at multiple locations in the trench, and not only in the main fault zone. Thus, potential events that could not be recognized at MM17 were probably captured elsewhere in the trench. Events E12 to E15 are good examples of this argument. The deformation associated to these events at MM17 is unclear, but numerous pieces of evidence were found elsewhere in the trench (Table 1, Fig. 4, Fig. S1).

3. Optically stimulated luminescence dating in Jbab el-Homr

3.1. Principle of luminescence dating

Given the dearth of organic material within the trench, we used luminescence dating to determine the age of the paleo-earthquakes recorded in the trench. Optically stimulated luminescence (OSL) techniques (Aitken, 1985, 1998; Rhodes, 2011) are used to determine the age of sediment burial. While buried, minerals, such as quartz and feldspar, are exposed to the ionizing radiation produced by the radioactive decay of ^{40}K and isotopes within the decay chain of ^{235}U , ^{238}U , and ^{232}Th , and they acquire a luminescence signal that increases as a saturating exponential with burial time. Any pre-deposition exposure of the minerals to daylight during transport ideally erased (i.e. bleached) the previous luminescence signal. For non-saturated samples, the age is expressed as the ratio of the dose received by the sample (i.e. paleodose or equivalent dose D_e , in Gy) over the dose delivered to the sample during burial (i.e. dose rate, in Gy/ka).

3.2. Sampling

In spite of the limestone-dominated local geology, quartz and feldspar minerals were identified by X-ray diffraction on a couple samples. These minerals are likely eolian, possibly coming from the Arabian Desert. Samples were collected for OSL dating in the 2009 trench. The layers identified in the 2003 trench were easily recognized in the 2009 trench based on visual appearance (Section 2.2, Figs. 3g, h, 4). The layers bracketing the paleo-earthquake horizons were sampled using 3.5-cm diameter PVC tubes driven into the trench wall (Fig. 3g, h), west of the main fault zone. In this study, we focused on 4 samples: JB2, JB17, JB37,

and JB47. Sample JB2 was collected just below the soil, at 50 cm depth and 40 cm above layer 6 (Figs. 3h, 4). Layer 4 was not observed in the sampling area. Assuming a similar sediment thickness between layers 6 and 4 in the sampling area and at MM17, sample JB2 would be located just below layer 4. Sample JB2 postdates event E3 and probably predates event E2. Sample JB17 was collected at 1.6 m depth, within layer 17, located between earthquake horizons E7 and E6. Sample JB37 was collected at 2.9 m depth, 2 cm above layer 38 and just below earthquake horizon E15. Sample JB47 was collected at 3.65 m depth, 10 cm below layer 46. It postdates event E17 and predates event E16.

3.3. Equivalent dose determination

3.3.1. Sample preparation

Luminescence dating was performed at the Department of Geosciences of National Taiwan University. For dating, we targeted both K-feldspars from polymineral assemblages and quartz, separated from the fine-grain fraction of the sample (Roberts, 2008). The luminescence sample was treated with HCl to dissolve carbonates, $\text{C}_2\text{Na}_2\text{O}_4$ to destroy mineral aggregates and H_2O_2 to remove organic matter. Then, the 4–11 μm grain size was isolated according to Stokes' law using a centrifuge (Frechen et al., 1996). At this stage, part of the polymineral sample material was mounted on aluminum discs by settling of a solution containing 2 mg of sample per aliquot suspended in acetone and used for dating.

The other part of the polymineral sample material underwent further chemical treatment using hydrofluorosilicic acid (H_2SiF_6) in order to isolate quartz by dissolution of the other minerals. We used a protocol adapted from Fuchs et al. (2005) and Roberts (2006). In a first step, silica sand was added to commercial H_2SiF_6 and left for 5 to 6 days in order to obtain a silica-saturated solution. The solution was filtered to remove the remaining silica grains. Then, the solution was mixed with the 4–11- μm polymineral samples using a sample-to-acid weight ratio of 40 during 3 days. The reaction duration was previously determined on test samples that were etched during 1 to 4 days and for which quartz purity was tested by infrared depletion test (Duller, 2003). The infrared depletion test was also conducted for samples used for dating to ensure the quartz purity (Table S1). The fine-grain quartz minerals were mounted on aluminum discs in the same way as polymineral aliquots.

3.3.2. Luminescence measurements and equivalent dose determination

The luminescence signal was measured on automated TL/OSL systems from Risø (TL-DA-15 and TL-DA-20) equipped with an infrared LED light source ($\lambda = 875 \text{ nm}$) and a blue LED light source ($\lambda = 470 \text{ nm}$) for optical stimulation and a photo-multiplier tube EMI 9235QB to count the emitted photons. The detection optics also comprised Schott BG-39 and Corning 7–59 filters when measuring polymineral aliquots and Hoya U340 filter when measuring quartz. Laboratory irradiation was done using $^{90}\text{Sr}/^{90}\text{Y}$ beta-sources delivering an annually calibrated dose rate of ~0.203 Gy/s and ~0.096 Gy/s on aluminum discs.

The equivalent doses were determined from three techniques: blue-green stimulated luminescence (BGSL) on quartz, and infrared-stimulated luminescence at 50 °C (IRSL) and post-IR stimulation at an elevated temperature of 225 °C (pIRIR₂₂₅) (Thomsen et al., 2008; Buylaert et al., 2009) on polymineral aliquots, the infrared-stimulated luminescence signal being dominated by K-feldspars (Bøtter-Jensen et al., 2003; Wintle, 2008). Contrary to IRSL, the pIRIR₂₂₅ technique has the

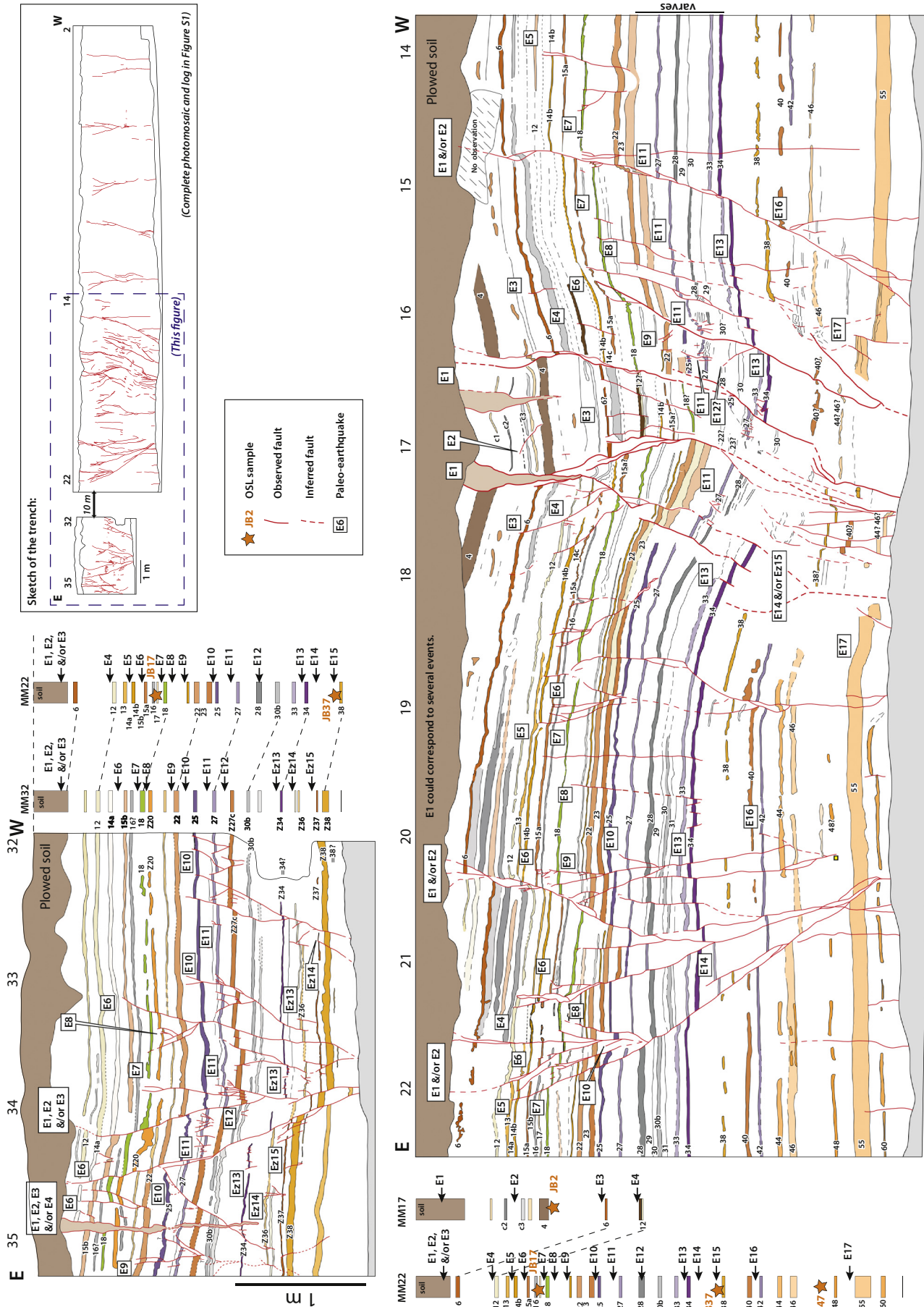


Fig. 4. Trench log focused on the eastern fault zone and main fault zone. Photomosaic and complete trench log are provided in Supplementary material (Fig. S1). Sketches of the stratigraphy on the side of the logs synthesize layer correlation across the trench and the relative positions of layers and earthquake horizons.

Table 1

Synthesis of evidence, stratigraphic position, and local size category for each event identified in the Jbab el-Homr trench. Size classification and uncertainties on event evidence are discussed in the main text (Section 2.3).

Event	Event size category	Synthesized description	Stratigraphic position	Description of evidences	Uncertainties in event evidence
E1	Large to very large	Few to numerous faults with >10 cm offset	Just below the plowed soil	Three cracks in the main fault zone at MM18–16 with ~50 cm down-drop of central block D (Fig. 5a). This deformation could correspond to several events post-dating deposition of layer 4. (Restoration in Fig. 5a)	The faults that reach the plowed soil at MM20–22 and MM15 could correspond to any of these events.
E2	Small to large	Single fault with limited offset to multiple faults with ~10 cm offset	Between layer c3 and layer c2	Only a crack at MM17 can be confidently associated to E2.	
E3	Medium	Numerous faults with limited offset	2 cm above layer 6	Multiple cracks in the main fault zone (MM16–18) and isolated cracks at MM14, MM11, MM6 and MM3	
E4	Medium	Numerous faults with limited offset	Just above layer 12	Multiple cracks in the main fault zone (MM21, MM18, MM16) and isolated cracks at MM9, MM6 and MM4	The down-drop of blocks B and C (Fig. 5a) could be related to any or all of these events.
E5	Small	Few faults with limited offset	Between layer 14a and layer 13	Few cracks in the main fault zone (MM22, MM19, MM14) and possibly an isolated crack at MM11	
E6	Large	Numerous faults with ~10 cm offset	Just above layer 15	Multiple cracks in the main fault zone (MM22–16) and in the eastern fault zone (MM33–35). 11-cm offset at MM16 and 3-cm vertical offset at MM33–35 (Restoration in Fig. 5b)	The faults that reach the plowed soil at MM20–22 and MM15 could correspond to any of these events.
E7	Medium	Numerous faults with limited offset	A few cm above layer 18	Multiple cracks in the main fault zone (MM22, MM20–19, MM15), in the eastern fault zone (MM34) and isolated cracks at MM14, MM6 and MM4.	
E8	Small	Few faults with limited offset	Above layers Z20 and Z22 and below layer 18	Few cracks in the main fault zone (MM22–19, MM16), in the eastern fault zone (MM33–34) and isolated crack at MM11 and MM6	
E9	Large	Numerous faults with ~10 cm offset	A few cm above layer 22	Multiple cracks in the main fault zone (MM22–20, MM–16), in the eastern fault zone (MM35) and isolated crack at MM11 and MM6. Offset increase for layers 22 and deeper on blocks Ea and Eb relative to blocks Ec and F and tilting of block A–B–C towards main fault zone at MM17 (Fig. 5b).	
E10	Medium	Numerous faults with limited offset	A few cm above layer 25	Multiple cracks in the eastern fault zone (MM32–35) and possibly in the main fault zone (MM22 and MM16)	
E11	Large	Numerous faults with ~10 cm offset	5 cm above layer 27	Multiple cracks in the main fault zone (MM20, MM18–16) and eastern fault zone (MM34–33) and isolated crack at MM13. Vertical offsets up to 7 cm at MM16. Varves allowed mapping flower structures in more details.	
E12	Small	Few faults with limited offset	Just above layer Z27c	Few cracks in the eastern fault zone (MM34, MM32). Light evidence within the main fault zone: crack at MM16.	
E13	Large	Numerous faults with limited to >10cm offset	Above layers 34 and Z34 and below layer 33	Multiple cracks in the main fault zone (MM20, MM16–18) and eastern fault zone and isolated cracks at MM13, MM9, MM6 and MM4. Vertical offset up to 10 cm of block C relative to block A–B.	
E14	Medium to very large	Numerous faults with ~10 cm offset or more	Above layers 38 and Z36, below layers 34 and Z34	Multiple cracks in the eastern fault zone (MM33–35) and a single crack at MM21.	
E15	Small to very large	Few faults with limited offset to multiple faults with >10 cm offset	Between layer Z38 and layer Z36	Few cracks in the eastern fault zone (MM33–35) only.	
E16	Small	Few faults with limited offset	Between layer 42 and layer 40	Few cracks at MM20, MM15 and MM11.	~30 cm down-drop of block C relative to block A and block E–F could be associated to one of these events or both.
E17	Large	Numerous faults with ~10 cm offset	Just above layer 55	Multiple cracks at MM19, MM16 and MM15. Vertical offset up to 15 cm at MM19. Layer 55 was dropped deeper than the trench bottom at MM16–18, preventing observations.	

advantage to have limited, often negligible, loss of luminescence signal with time (i.e. anomalous fading; Huntley and Lamothe, 2001). However, the pIRIR₂₂₅ signal requires longer exposure to daylight to be bleached and a small residual dose (< 1% of the natural dose) remains after a day of light exposure (Kars et al., 2014; Colarossi et al., 2015). Because the samples come from the fine-grain fraction of low energy deposits, with a possible eolian origin, efficient bleaching seems likely.

For each technique, we used a single aliquot regeneration (SAR) protocol (Murray and Wintle, 2000) with five regeneration dose points, including a zero point and a recycling point. The measurement parameters are shown in Table 2. The reliability of the protocols was successfully tested with preheat temperature tests and dose recovery tests on 4–5 aliquots per sample (Fig. S2). For the pIRIR₂₂₅ technique, 7 aliquots per sample were bleached during 4 h in a solar stimulator (Dr. Hönle SOL2), 4 of them were used for the dose recovery test and the other 3 for measurement of the residual dose (Fig. S3). To calculate the

pIRIR₂₂₅ dose recovery ratios, the average residual dose obtained from a given sample was subtracted from the doses recovered from the aliquots used for the dose recovery test. The residual dose was not subtracted from the natural dose since it may not be representative of the residual dose when the minerals were buried. For all techniques, we obtained dose recovery ratios within the acceptance range of 1.0 ± 0.1 (Figs. S2, S3).

The minerals showed high natural signal with characteristic shine-down curves decaying within few seconds for quartz and within a few tens of seconds for K-feldspars (Fig. S4). The SAR measurements performed for equivalent dose determination showed natural signals below saturation, dose response curves with good quality fits (Fig. S4) and limited changes in sensitivity during the sequence cycles (Wintle and Murray, 2006). Recycling ratios were within 1.0 ± 0.1 and recuperation values lower than 5% for all the measurements. For each technique, equivalent dose measurements of 8 to 29 aliquots per sample led

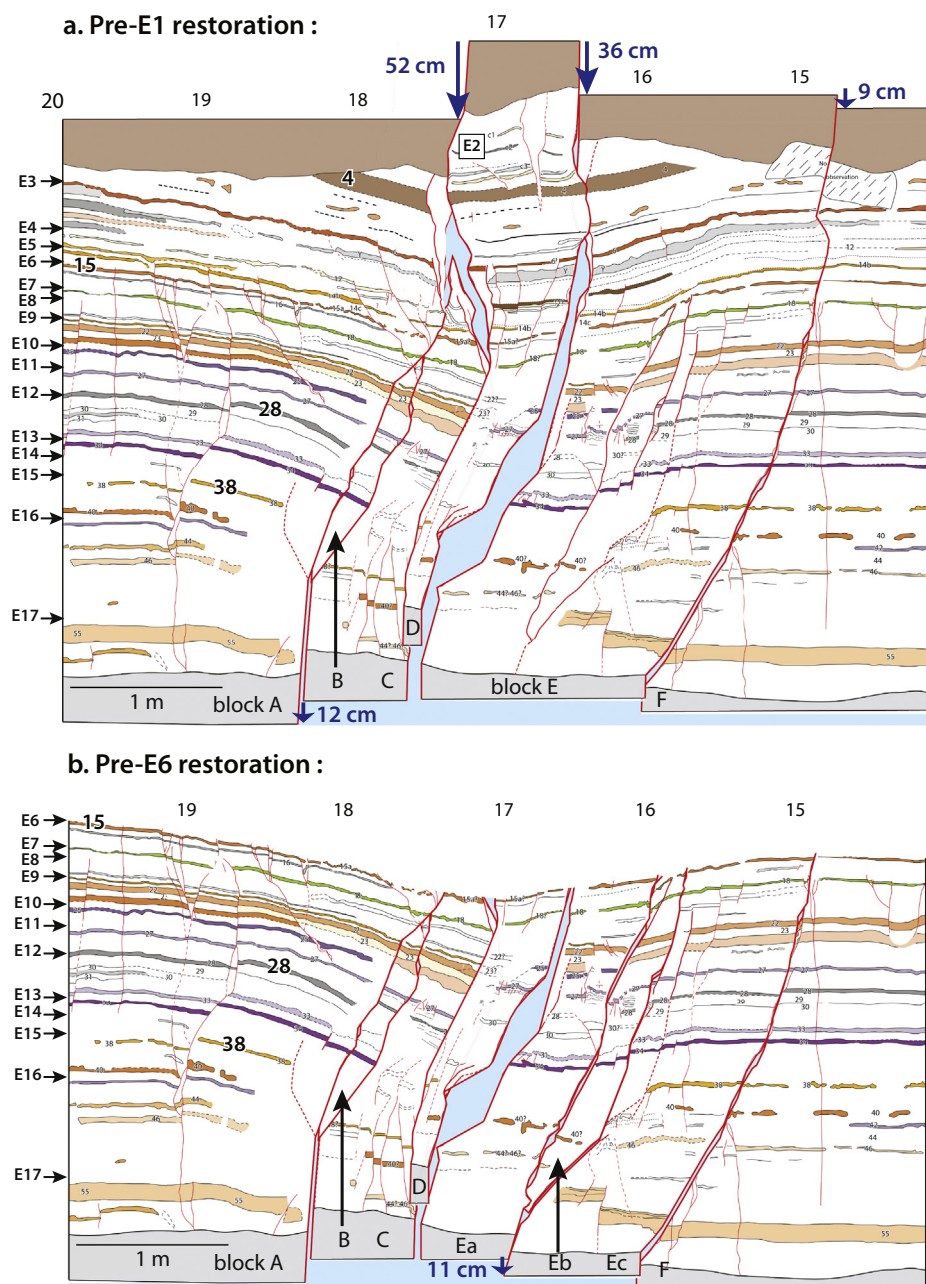


Fig. 5. Restoration of the stratigraphy to its geometry before events E1 and E2 (layer 4 restored) (top) and before event E6 (layer 15a restored) (bottom). The main cracks associated with these events are used to define blocks labeled A to F. Restorations help quantifying the deformation associated to individual events and assessing remaining deformation related to older events. They also highlight the variable offsets related to each event. Top: The main deformation feature is the ~ 50 cm down-drop of block D. We also restored layers 14b to 28 across blocks A, B and C, although this deformation could have occurred during any or all events E1 to E5. Bottom: The main deformation associated to E6 is the ~ 11 cm down-drop of block Ea relative to Ec. Note that the stratigraphic horizon of E7 is nearly restored, showing that E7 generated minor deformation.

to fairly clustered dose distributions (Fig. 6, Fig. S5). Using the central age model of Galbraith et al. (1999), we obtained the equivalent doses reported in Tables 3 and 4.

3.3.3. Fading rates

For the IRSL and the pIRIR₂₂₅ techniques, we quantified the fading rate, represented by the g-value in % per decade, based on Auclair et al. (2003) and using 8 to 12 aliquots per sample. Time delays between irradiation and measurements reached ~ 40 to ~ 100 h for IRSL and ~ 75 – 85 h for pIRIR₂₂₅ (Fig. S6). For IRSL, g-values from individual aliquots of a given sample were consistent with each other (Fig. S6) and we obtained average g-values from 3.2 ± 0.4 to $4.0 \pm 0.2\%$ /decade (Table 4). For pIRIR₂₂₅, we obtained slightly different g-values for the two samples, with $2.5 \pm 0.5\%$ /decade for JB2 and $1.6 \pm 0.4\%$ /decade (Table 4, Fig. S6). The fading correction was performed using the function provided in the R luminescence package (Fuchs et al., 2015).

3.4. Environmental dose rates

The annual dose rates were derived from the concentrations of U, Th, and K in the sediment, the sediment water content, and the contribution from cosmic rays. The concentrations of U and Th were measured by ICP-MS and the percentage of K was measured by X-ray fluorescence (Table S2). We obtained present-day water contents of 7–10%. However, because the water content was likely higher in the past and varied according to paleoclimatic conditions and sediment compaction, we considered a value of $15 \pm 10\%$. The dose rates were calculated using the DRAC calculator (Durcan et al., 2015; version 1.2) based on conversion factors from Guérin et al. (2011), using a-values of 0.086 ± 0.016 for polymineral samples and 0.04 ± 0.01 for quartz (Rees-Jones, 1995) and assuming a K content of $12.5 \pm 0.5\%$ for the K-feldspar internal dose rate (Huntley and Baril, 1997). The contribution from cosmic rays was calculated based on Prescott and Hutton (1994), considering a sediment density of 2 g/cm^3 . The environmental dose rates are given in Tables 2, 3 and Table S2.

Table 2

Sequence descriptions for the three techniques, blue-green stimulated luminescence (BGSL) on quartz and infrared stimulated luminescence at 50 °C (IRSL) and post-infrared infrared stimulated luminescence at 225 °C (pIRIR₂₂₅) from polymineral assemblages.

Steps	BGSL (quartz)	IRSL (polymineral)	pIRIR ₂₂₅ (polymineral)
1	Dose	Dose	Dose
2	Preheat at 180 °C for 10 s	Preheat at 180 °C for 60 s	Preheat at 320 °C for 60 s
3	BGSL at 125 °C for 40 s	IRSL at 50 °C for 300 s	IRSL at 50 °C for 100 s
4	Test dose	Test dose	IRSL at 225 °C for 200 s
5	Preheat at 180 °C for 10 s	Preheat at 180 °C for 60 s	Test dose
6	BGSL at 125 °C for 40 s	IRSL at 50 °C for 300 s	Preheat at 320 °C for 60 s
7	Return to Step 1	Return to Step 1	IRSL at 50 °C for 100 s
8			IRSL at 225 °C for 200 s
9			Return to Step 1

Table 3

Summary of luminescence dating results for BGSL on quartz. Dose rates were calculated using the DRAC software (version 1.2; Durcan et al., 2015; www.aber.ac.uk). See text and Table S2 for details on the environmental dose rate calculation.

Sample ^a	Depth (m)	n ^b	De ^c (Gy)	Dose rate (Gy/ka)	Age (ka)
JB2	0.5	17	65.27 ± 0.75	2.43 ± 0.18	26.9 ± 2.3
JB17	1.6	8	71.30 ± 1.20	2.38 ± 0.24	29.9 ± 3.5
JB37	2.9	18	80.10 ± 1.00	2.73 ± 0.24	29.3 ± 3.0
JB47	3.65	15	88.47 ± 1.13	2.88 ± 0.23	30.8 ± 2.9

^a Location: N34.3397° E36.2128°, 1820 m in elevation.

^b Number of aliquots used to determine the equivalent dose De.

^c Equivalent doses and errors are calculated using the Central Age Model (Galbraith et al., 1999).

3.5. Age results and discussion

Ages are summarized in Tables 2 and 3 and in Fig. 7. From BGSL on quartz, we obtained ages of 26.9 ± 2.3 ka for JB2, 29.9 ± 3.5 ka for JB17, 29.3 ± 3.0 ka for JB37, and 30.8 ± 2.9 ka for JB47. From IRSL on polymineral aliquots, we obtained fading-corrected ages of 18.2 ± 1.6 ka for JB2, 19.5 ± 2.3 ka for JB17, 19.2 ± 1.9 ka for JB37, and 21.3 ± 1.9 ka for JB47. For both techniques, the ages consistently increase with depth and cover a similar time lapse of ~3–4 ka, with JB17 and JB37 being indistinguishable given uncertainties. Both sets of ages lead to similar average sedimentation rates of 0.94 ± 0.78 (1σ) mm/a for BGSL and 1.25 ± 1.10 (1σ) mm/a for IRSL (Fig. 7). However, the IRSL ages are significantly younger than the BGSL ages, with a systematic age difference of 9–10 ka. From the pIRIR₂₂₅ technique, on polymineral aliquots, we obtain indistinguishable fading-corrected ages of 26.1 ± 2.5 ka for JB2 and 25.7 ± 2.5 for JB47 (Table 3, Fig. 7). The pIRIR₂₂₅ age of JB2 matches well with the BGSL age, while the pIRIR₂₂₅ age of JB47 lies in-between the BGSL and IRSL ages, with uncertainties overlapping with the BGSL age. Hence, the pIRIR₂₂₅ ages support the BGSL ages rather than the IRSL ages.

Due to the fair agreement between BGSL ages and pIRIR₂₂₅ ages in this study, we consider those age sets more reliable than the IRSL ages. Yet, the IRSL data that we collected do not suffer from any obvious flaw or weakness that could explain the age discrepancy and argue for rejection of the IRSL ages. The systematic age difference towards younger IRSL ages compared to BGSL suggests that the fading correction or the g-values determination might be an issue for those IRSL samples. Fading correction for IRSL generally led to satisfactory agreement with independent ages in many cases (e.g. Huntley and Lamothe, 2001; Lamothe et al., 2003; Buylaert et al., 2008; Kars and Wallinga, 2009). However, a few studies reported discrepancies between fading-

Table 4 Summary of luminescence dating results for IRSL and pIRIR₂₂₅ on K-feldspar. Dose rates were calculated using the DRAC software (version 1.2; Durcan et al., 2015; www.aber.ac.uk). The fading-correction was performed using the function provided in the R luminescence package (Füchs et al., 2015). See text and Table S2 for details on the environmental dose rate calculation.

Sample	n ^a	De ^b (Gy)	Dose rate (Gy/ka)	g-Value (%/decade)	Uncorrected age (ka)	Fading-corrected age (ka)
IRSL (polymineral)						
JB2	19	42.00 ± 0.33	2.87 ± 0.23	3.19 ± 0.38	14.7 ± 1.2	18.2 ± 1.6
JB17	29	43.94 ± 0.27	2.83 ± 0.31	3.28 ± 0.28	15.5 ± 1.7	19.5 ± 2.3
JB37	24	46.89 ± 0.45	3.23 ± 0.31	3.98 ± 0.15	14.5 ± 1.4	19.2 ± 1.9
JB47	19	57.14 ± 0.46	3.40 ± 0.29	3.45 ± 0.35	16.8 ± 1.4	21.3 ± 1.9
pIRIR ₂₂₅ (polymineral)						
JB2	12	63.34 ± 0.61	2.87 ± 0.23	2.46 ± 0.46	22.1 ± 2.0	26.1 ± 2.5
JB47	13	78.72 ± 0.76	3.40 ± 0.29	1.61 ± 0.37	23.1 ± 2.2	25.7 ± 2.5

^a Number of aliquots used to determine the equivalent dose De.

^b Equivalent doses and errors are calculated using the Central Age Model (Galbraith et al., 1999).

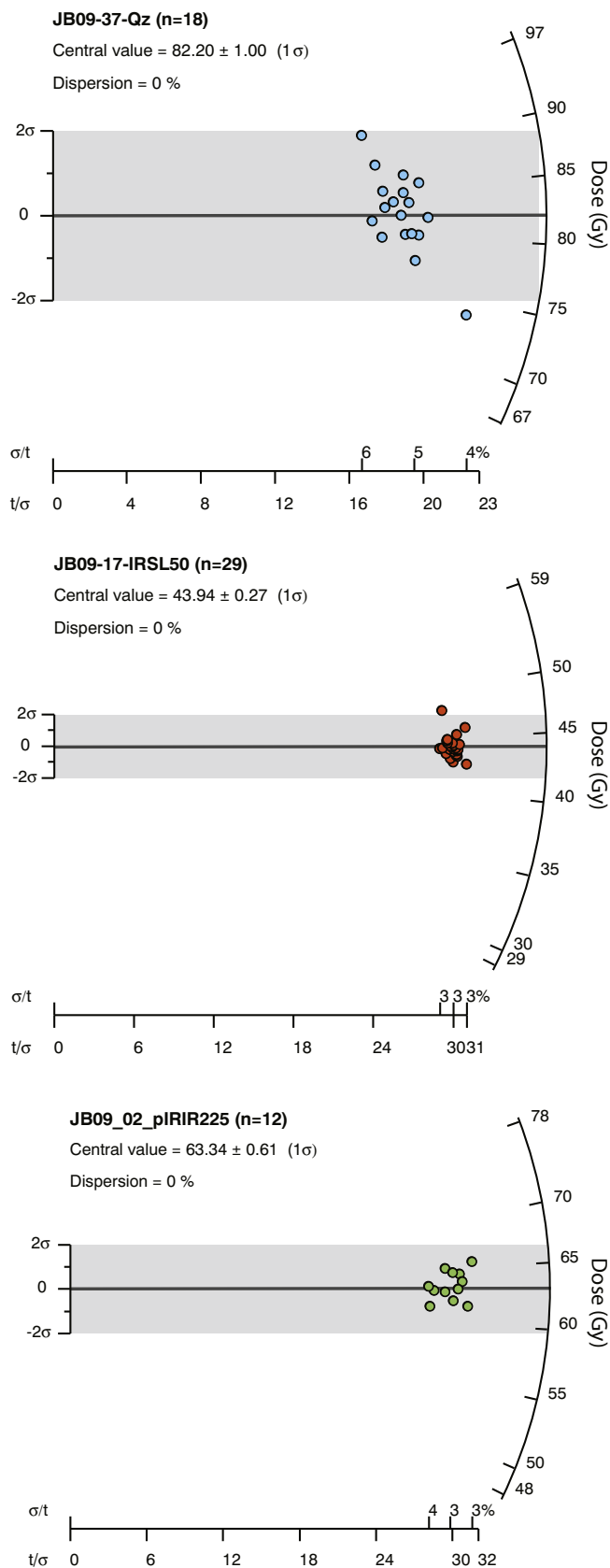


Fig. 6. Examples of equivalent dose D_e distribution for one quartz sample (BGS), one IRSL sample, and one pIRIR₂₂₅ sample. Radial plots of the other samples and techniques are shown in Supplementary Fig. S5. n indicated the number of aliquots used to calculate equivalent doses and errors, based on the Central Age Model (Galbraith et al., 1999).

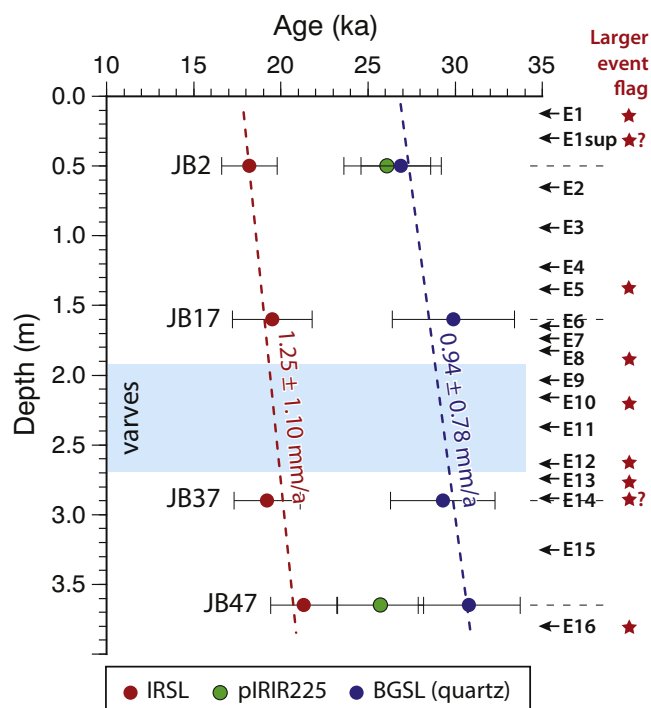


Fig. 7. Synthesis of luminescence ages and earthquakes as a function of depth. Regression lines indicate best-fit sedimentation rates with 1σ uncertainty. Red stars indicate larger events (Table 1) based on deformation amplitude. Blue shade shows the stratigraphic position of the varves. (For interpretation of the references to color in this figure legend, the reader is referred to the web version of this article.)

corrected IRSL ages and expected ages based on independent techniques, questioning the representativeness of the g -values at the geologic timescale and possibly the robustness of the measurement protocol (Wallinga et al., 2007; Kars and Wallinga, 2009; Reimann et al., 2011). In this line, we hypothesize that the g -values that we determined for IRSL may be underestimated. Further analytical work would be necessary to explore this possibility. The g -values required to obtain IRSL ages similar to the quartz ages are comprised between 7.1 and 7.9%/decade, which is about twice the values that we obtained (3.2 to 4.0%/decade).

To summarize, we favor the BGS and pIRIR₂₂₅ ages over the IRSL ages, mainly based on their fair agreement. We also favor the BGS ages over the pIRIR₂₂₅ ages, because BGS ages do not involve as many assumptions, regarding bleaching, residual dose and fading rate. In the following discussion, we will rely on the BGS ages and on the sedimentation rate derived from them.

4. Discussion

4.1. Sedimentary record and paleo-environments

In this section, we summarize the characteristics of the Jbab trench sedimentary record and we discuss a possible succession of paleo-environments consistent with this record and with local paleoclimatic studies.

Luminescence dating led to BGS ages from fine-grain quartz from ~26.9 ka at 0.5 m depth to ~30.8 ka at 3.65 m depth (Table 3). The thin clayey and silty layers deposited during this period strongly suggest deposition in a marsh or shallow lake (Fig. 2a). This is also supported by the flat morphology of the basin. The stratigraphy includes a ~0.9-m thick varve sequence (Fig. 3d). Varves counting led to 125 years of sedimentation assuming that they correspond to a seasonal cycle. However, layers with different characteristics are intercalated within

the varve sequence and they could represent longer deposition times. The lack of temporal resolution in the OSL ages prevents us from discussing further the duration represented by the varve sequence. Although varves may have various compositions reflecting a large variety of sedimentary processes and climatic conditions, the clayey varves of Jbab recall the seasonal varves observed in proglacial lakes of Europe and North America (e.g. Reading, 1996; Ojala et al., 2012; Zolitschka et al., 2015). The stratigraphic sequence ends upward with a poorly developed plowed soil that likely formed rapidly. The restoration of the strata prior to event E1 (Fig. 5a) strongly suggests that the upper part of the stratigraphic sequence (layer 4 and above) has been eroded away. Therefore, a significant length of time, possibly up to ~25 ka, is probably missing at the top of the trench exposure. To summarize, the sedimentary record of the Jbab trench indicates a dramatic change in sedimentary environment, from a marsh or intermittent shallow lake, possibly proglacial, during the period ~26.9 to ~30.8 ka, to a landscape with limited sediment transport, if any, and even some erosion since possibly ~25 ka.

The evolution of the sedimentary environment in Jbab likely reflects local paleoclimatic variations. The ages that we obtained are significantly older than the Holocene sequence that one could expect from the bottom of an intra-mountainous basin. Instead, they correspond well with the beginning of the Last Glacial Maximum (LGM) at 29 ka (Lisiecki and Raymo, 2005). Earlier studies proposed the presence of glaciers on Mount Lebanon during the LGM on the basis of horseshoe-shape cirques and U-shaped valleys on the west flank of Mount Lebanon, where ^{36}Cl cosmogenic dating of moraines down to ~1950 m elevation led to 18–20 ka ages (Messerli, 1966; Daëron, 2005; Moulin et al., 2011). Based on paleo-environment proxies from cores of the Yammouneh basin, located 30 km south (Fig. 1b), at 1350 m elevation, Develle et al. (2010, 2011) and Gasse et al. (2011, 2015) describe extremely dry conditions during the LGM, in particular during the period 16–21 ka, due to low precipitation or storage of water as ice in glaciers and snow. These conditions certainly applied to Jbab too, as it is located at higher elevation (1820 m) than Yammouneh. Therefore, the presence of a proglacial lake in Jbab at the beginning of the LGM seems possible. The lack of sedimentation in Jbab after ~25 ka may be explained by the frozen landscape suggested by Develle et al. (2010, 2011) and Gasse et al. (2011, 2015). At the end of the LGM, pollens from the Yammouneh basin indicate a fairly rapid transition towards warmer and wetter conditions that prevailed until the early Holocene (Gasse et al., 2015). A lake remained in the Yammouneh basin until it was artificially drained in the 20th century. The lack of sedimentary record after the LGM in Jbab indicates the absence of any significant water body that would trap the clasts and/or that part of the stratigraphic sequence has been eroded. Because Jbab is a closed intra-mountainous basin, the only erosive agent possible is the wind.

4.2. Earthquake chronology and tentative implications for past surface rupture preservation and fault zone evolution

4.2.1. Earthquake chronology and recurrence intervals in Jbab el-Homr compared to Yammouneh

The relatively old ages and associated uncertainties that we obtained do not allow discussing the timing of individual earthquakes and the recurrence intervals between successive events. Hence, we look at the average recurrence interval of ground rupturing events and their distribution in the stratigraphy. In doing so, we first consider all the events, regardless of their size, and then focus only on the larger ones (Table 1; Section 2.3). We then compare the earthquake chronology in Jbab with the record at the Yammouneh site, located 30 km south (Daëron et al., 2007). We focus here on the time period between 26.9 ka and 30.8 ka. The earthquake activity since 26.9 ka will be discussed in Section 4.2.3.

In a first step, we examine the earthquake chronology in Jbab regardless of the events size. We identified 14 events, E3 to E16, between

26.9 ± 2.3 ka (sample JB2) and 30.8 ± 2.9 ka (sample JB47) (Figs. 4, 7). These ages cover a period of 3.9 ka considering the central age values, with lower and upper bounds of 0 to 9.1 ka considering uncertainties. This leads to an average recurrence interval of 280 years, with a lower bound of 0 and an upper bound of 650 years.

We note that the stratigraphic positions of the earthquake horizons are not evenly distributed with depth (Figs. 4, 7). Events are more numerous between JB17 and JB37 (9 events within 1.3 m thickness) than between JB2 and JB17 (4 events within 1.1 m thickness) and between JB37 and JB47 (1 event only within 0.75 m thickness, but with limited observation capabilities). Assuming a constant sedimentation rate of 0.94 mm/a (Fig. 7) would make earthquakes twice more frequent between JB17 and JB37 (~150 years recurrence) than between JB2 and JB17 (~290 years recurrence). A faster sedimentation rate during the interval JB17–JB37 seems likely, as this interval includes potentially seasonal varves and led to undistinguishable ages, and faster sedimentation would make earthquakes appear even more frequent during this interval. Therefore, the distribution of event horizons along the stratigraphy likely reflects temporal clustering of earthquakes.

In a second step, we focus only on the events considered as larger based on relative deformation amplitude (Section 2.3; Table 1; Fig. 7). In this case, 5 to 6 larger events were identified between JB2 and JB47, i.e. during 3.9 ka ([0; 9.1 ka]), leading to an average recurrence interval of 720 years, constrained between 0 and 1670 years.

The earthquake chronology of the Jbab trench can be compared with the record of the Yammouneh trench, located 30 km south (Fig. 1b). Regardless of possible differences in event magnitude, the average recurrence interval in Jbab (280 years [0; 650 years]) is a lot shorter than the average recurrence interval of 1127 ± 135 years determined in Yammouneh during the period 6.4–12.0 ka (Daëron et al., 2007). Focusing on the larger events of Jbab seems to roughly reconcile both records, keeping in mind the large uncertainty on the Jbab recurrence time (720 years [0; 1670 years]).

4.2.2. Reconciling the Jbab and Yammouneh paleo-earthquake records

Considering all events, the average recurrence interval of ground rupturing events is significantly shorter at the Jbab site than at the Yammouneh site, while the sites are located only 30 km apart. In this section, we propose three possible explanations to reconcile these records: the different stratigraphic resolution at each site, the segmentation of the fault, and temporal variations in the earthquake activity.

An outstanding characteristic of the Jbab trench is the high resolution of the stratigraphy, from 1 to 5 cm thick layers down to millimetric laminae (Fig. 3). Detailed stratigraphy allows distinguishing past ruptures separated by a thin layer representative of a short time span, while these ruptures may appear as a single one in a rougher or slower sedimentation setting. Detailed stratigraphy also allows preserving small, centimeter-scale deformations, possibly related to smaller-magnitude events ($M = 6.0$ – 6.5 or possibly even less) or to smaller coseismic slip at the tips of the rupture. These small deformations would likely be missed if located within a thicker homogeneous layer. Therefore, given a series of ground rupturing events of various sizes, a trench with higher stratigraphic resolution will likely have recorded all the events, while a trench with lower stratigraphic resolution will have preserved only the larger events and some of the medium-size events, leading to an apparent shorter average earthquake-recurrence time than for the higher stratigraphic resolution trench.

The way stratigraphic resolution affects paleo-earthquake detection capabilities may introduce flaws in the interpretation of trenches. Firstly, if the stratigraphic resolution changes within a given trench, the higher detection capabilities within the section with thinner strata may lead to apparent temporal clustering of earthquakes. Secondly, comparing the earthquake record from trenches located at different sites and with uneven stratigraphic resolution may not be straightforward. This is likely to be the case for the Jbab and the Yammouneh sites. At Jbab, 7 to 10 events out of 17 are associated with centimeter-scale

deformations recorded in mainly 0.1 to 1 cm-thick layers. By contrast, most layers in the Yammouneh trench are 5–10 cm thick or more (Daëron et al., 2007). Hence, a basic event count would indeed lead to a longer recurrence interval at Yammouneh compared to Jbab. Alternatively, we attempt to account for the magnitude of the recorded events and propose that the events that were identified in the Yammouneh trench were as large as the larger events identified in Jbab. This threshold is motivated by the similarity between the vertical offsets generated by larger events (≥ 10 cm) in Jbab and the layers thickness in Yammouneh (≥ 5 –10 cm). Then, the 720-year ([0; 1670 years]) recurrence interval of larger events in Jbab is compatible with the 1127 ± 135 years recurrence time determined in Yammouneh.

Multiple lines of evidence exist for ground surface ruptures associated to $M < 6.5$ events (see Liu-Zeng et al. (2015) for a review). To date, only a few studies reported evidence for smaller-magnitude ($M \sim 5.8$ –6.5) events identified in paleoseismic trenches across strike-slip faults (Liu-Zeng et al., 2007, 2015; Streig et al., 2014). The difficulties in estimating paleo-earthquakes magnitude and the scarcity of favorable sedimentary environments clearly limit the number of such studies. The Jbab trench site appears highly favorable to preserve small deformation, related to $M \sim 6.0$ –6.5 or possibly even smaller events. In spite of numerous limitations and uncertainties, the fact that focusing only on the larger events nearly matches the Yammouneh fault record supports the idea that both records differ due to uneven stratigraphic resolution. Yet, it is not the only possible cause: fault segmentation and earthquake clustering may also influence local earthquake records.

Large continental strike-slip faults have long been recognized to consist in fairly linear segments separated by bends and step-overs that play a role in the initiation and termination of earthquake ruptures (e.g. King and Nabelek, 1985; Wesnousky, 2006; Klinger, 2010). Hence, trench sites located in the central part of one segment may record events that rupture only that segment and events that rupture multiple segments. Also, a trench site located close to or at a boundary between two segments may record ruptures involving only one of the two segments located on each side of the boundary and also events breaking through the boundary to rupture multiple segments.

If one examines the Yammouneh fault trace in the vicinity of the Yammouneh trench site, from north to south the fault is fairly linear, cross-cutting the pull-apart basin, with the nearest significant bend located ~ 5 km north of the trench. Thus, we consider that the Yammouneh site corresponds to the central part of a fault segment. Conversely, the Jbab site is located within a fault bend as the fault veers northward by 20° ~ 1 km south of the trench, and veers back eastward by 15° ~ 2.5 km north of the trench. Hence, the Jbab trench is likely located at the boundary between two fault segments, recording ending ruptures on one segment or the other, as local small events, and ruptures that affected at least both segments together and generated locally larger deformation.

The third possible cause for different recurrence interval in Jbab and Yammouneh is related to possible irregular distribution of earthquakes through time, during active clusters separated by periods of seismic quiescence (e.g. Scholz, 2002; Zielke et al., 2015). The records from Jbab and Yammouneh cover different time periods, 26.9–30.8 ka and 6.4–12.0 ka for Jbab and Yammouneh respectively, and also have a different duration. Therefore, both records could simply differ due to temporal variations in the earthquake cycle.

The results of several regional paleoseismological studies allow evaluating the possibility of temporal clustering of earthquakes on the Dead Sea fault (see Wechsler et al. (2014) and Lefevre et al. (2018) for a review; Fig. 1). Along the Yammouneh fault, Daëron et al. (2007) determined recurrence intervals for a subset of 6 events between 6.4 and 12.0 ka, but the large uncertainties did not allow arguing for periodicity or clustering. Based on trenches and archeological investigations along the Jordan Valley fault, Ferry et al. (2011) obtained a 14-ka-long record affected by hiatuses. They determined recurrence intervals between each event that vary from 280 years to 1500 years, therefore rather

arguing for temporal clustering. Based on a shorter record of the last ~ 2 ka on the Jordan Gorge fault, Wechsler et al. (2014, 2018) found evidence for only 2 events during the last millennium, but for 7 events during the previous millennium, when the fault slip rate was twice faster than the ~ 2 -ka mean slip rate. As mentioned by the authors, this cluster is likely related to the peculiar location of the Jordan Gorge fault, at the junction between several faults (Fig. 1), so that this record may not be representative of the seismic behavior of fault segments in a more simple structural setting. Further south, on the Wadi Araba fault (Fig. 1), Klinger et al. (2015) and Lefevre et al. (2018) also observed earthquake clustering during the last 2 ka, with recurrence intervals varying between 144 years and ~ 700 years. Marco et al. (1996) investigated longer-term coseismic deformations observed from numerous exposures of the Late Pleistocene lacustrine Lisan formation in the southern part of the Dead Sea basin. They derived 10-ka cycles of earthquake clustering and quiescence, attributed however to a secondary fault zone. To summarize, previous paleoseismological studies do not permit to evaluate the temporal pattern of earthquakes on the Yammouneh fault itself, but studies conducted on other sections of the Dead Sea fault support temporal earthquake clustering at the millennial timescale during the Holocene. If this behavior extended to the Yammouneh fault, it may explain the different average recurrence intervals determined at the Jbab and Yammouneh sites.

4.2.3. Earthquake activity since 26.9 ka and possible fault zone migration

We find evidence for a minimum of two events within the trench since ~ 26.9 ka, E1 and E2 (Section 2.3; Table 1). The lack of sedimentary record since ~ 26.9 ka and the termination of the most recent faults within the plowed soil prevent constraining the timing of the most recent earthquake recorded in the Jbab trench. We discussed in Section 2.3 (Table 1) that faults and deformation associated to event E1 could represent several events. In the following, we estimate the number of events that E1 may represent under the assumption that the fault behavior during the time period ~ 26.9 –30.8 ka is representative of the fault behavior since ~ 26.9 ka and we discuss the implications.

Under this assumption, about one event out of two generates ~ 10 -cm vertical offset and the other event generates ≤ 1 -cm vertical offset. Then, the ~ 50 -cm down-drop associated to event E1 at MM17 (Fig. 5a) would represent about 10 events since ~ 26.9 ka, leading to a long average recurrence interval of ~ 2.7 ka. Such return time is not supported by any previous paleoseismological study along the Yammouneh fault (Daëron et al., 2007), along adjacent faults in southern Syria and northern Israel (Meghraoui et al., 2003; Wechsler et al., 2014; Ellenblum et al., 2015), or further south (Ferry et al., 2011; Klinger et al., 2015; Lefevre et al., 2018).

We then need to explain why earthquakes seem to be missing in Jbab during the last ~ 26.9 ka compared to elsewhere on the fault. We propose that the missing events occurred on another branch of the fault. A possible additional fault branch is inferred from high-resolution satellite images from Google Earth, in particular those shot on 06/11/2005 and 10/23/2005 (Fig. 2b), therefore not available when the 2003 trench was excavated. West of the excavated fault branch and parallel to it, these images show a linear boundary between a slightly lower western block, with darker soil or more vegetation or flooded, and a higher eastern block that mostly remains dry. Including this additional fault branch, the width of the Yammouneh fault zone in the Jbab basin would reach ~ 110 m. Active fault maps show that fault traces are wide and complex at geometric irregularities, such as bends and step-overs of various spatial scales (e.g. Aviles et al., 1987; Okubo and Aki, 1987; Klinger, 2010; Le Béon et al., 2012). The widening of the fault zone in Jbab is likely favored by the 20° change in fault azimuth across the basin (Fig. 2). To explain the lack of earthquakes along the eastern branch of the fault since ~ 26.9 ka, we hypothesize that the fault activity migrated gradually from the eastern branch to the western branch. New excavations are required to test the existence of this inferred fault.

If we now assume that the earthquake activity was clustered in time

during the last ~30.8 ka, the fault behavior during ~26.9–30.8 ka would represent an earthquake cluster and simply cannot be extrapolated to the last ~26.9 ka. Then, the question of the number of events that E1 represents remains open. Considering the recurrence interval of 1127 ± 135 years determined at the Yammouneh site (Daëron et al., 2007), about 24 earthquakes would have happened since ~26.9 ka at Jbab. The deformation associated to events E1 and E2, within the main fault zone, but also as isolated cracks away from the main fault zone, seems too limited to represent so many events. Therefore, we seriously consider the possibility of the existence of another fault branch.

5. Conclusions

We investigated a paleoseismological record that spans the last ~30.8 ka. The Jbab trench revealed at least 17 events, well constrained by ruptures within very thin (0.1–5 cm) stratigraphic units. Fourteen events were dated between 26.9 ± 2.3 ka and 30.8 ± 2.9 ka, based on luminescence dating on fine-grain quartz. The earthquake chronology since ~26.9 ka remains uncertain due to missing stratigraphy. The variability of coseismic deformation associated to each event suggests events of variable size, with 7 to 10 out of 17 events considered as larger events, associated with vertical offsets larger than 10 cm. Considering all events regardless of their size, we determined a mean recurrence interval of 280 years ([0; 650 years]) that is significantly shorter than the return time determined at the Yammouneh trench site (1127 ± 135 years), located 30 km south (Daëron et al., 2007). We propose three explanations that may all have played some role in the origin of such different records. First, the Jbab and Yammouneh records may differ due to the difference of location of the two sites relative to the fault segmentation, with Jbab being located within a fault bend, while Yammouneh is located on the central portion of a fault segment. Second, since the two records cover different time periods (6.4–12.0 ka for Yammouneh and 26.9–30.8 ka for Jbab), they may reflect temporal clustering of earthquakes. The third explanation involves the recording capabilities of the sites in relation to the thickness of the layers exposed in the trench. The higher stratigraphic resolution in Jbab compared to Yammouneh likely enables recording small events ($M = 6.0$ – 6.5 or less) associated with ~1-cm-scale deformation, while such deformation is not easily identified within the thicker strata of the Yammouneh site. Indeed, both records are nearly reconciled when only the larger events recorded in Jbab are considered, leading to a 720-year-long return time ([0; 1670 years]), and suggesting that stratigraphic resolution may be the main factor responsible for the different paleoseismic records.

The possibility for paleoseismic trenches to record, under favorable conditions, smaller-magnitude events makes such record harder to interpret in term of fault seismic behavior. Indeed, smaller $M \sim 6.0$ – 6.5 events and larger $M > 7$ events bear different significance in term of stress release and slip budget on the fault plane. This emphasizes the need to combine earthquake time series with local coseismic slip data, although appropriate markers are not always available. Such detailed records of paleo-earthquakes are precious for seismic hazards assessment. Indeed, smaller-magnitude ground-rupturing events likely nucleate at relatively shallower depths and still represent a significant hazard for local populations and infrastructures.

Supplementary data to this article can be found online at <https://doi.org/10.1016/j.tecto.2018.04.009>.

Acknowledgements

We thank the National Center for Geophysical Research of Lebanon and the American University of Beirut for their valuable administrative assistance and help in the field during the 2003 and 2009 campaigns, as well as the multiple fieldwork helpers (Michel Aoun, Faten Khatib, Myrtille Kupermink). We are grateful to Prof Yue-Gau Chen for allowing access to the Luminescence Dating Laboratory of National Taiwan University and to two anonymous reviewers whose comments

helped improving our manuscript. This research benefitted from financial support by the National Center for Geophysical Research of Lebanon (GRP08 grant to AE), the Institut National des Sciences de l'Univers of France, the Ministry of Science and Technology of Taiwan (grant MOST104-2116-M-008-025-MY3 to MLB), and the French Ministère des Affaires Étrangères. MLB also wishes to thank Prof. John Suppe for financial support during the 2009 field campaign.

References

- Aitken, M.J., 1985. Thermoluminescence Dating. Academic Press, London.
- Aitken, M.J., 1998. An Introduction to Optical Dating. Oxford University Press, Oxford.
- Akçiz, S.O., Ludwig, L.G., Arrowsmith, J.R., Zielke, O., 2010. Century-long average time intervals between earthquake ruptures of the San Andreas fault in the Carrizo Plain, California. *Geology* 38, 787–790.
- Ambraseys, N., 2009. Earthquakes in the Mediterranean and Middle East: A Multidisciplinary Study of Seismicity up to 1900. Cambridge University Press.
- Ambraseys, N.N., Melville, C.P., Adams, R.D., 1994. The Seismicity of Egypt, Arabia and the Red Sea (173 pp.). Cambridge University Press, Cambridge.
- Auclair, M., Lamothe, M., Huot, S., 2003. Measurement of anomalous fading for feldspar IRSL using SAR. In: Proc. 10th Int. Conf. Lumin. Electron-Spin Reson. Dating LED 2002 37, pp. 487–492. [http://dx.doi.org/10.1016/S1350-4487\(03\)00018-0](http://dx.doi.org/10.1016/S1350-4487(03)00018-0).
- Aviles, C.A., Scholz, C.H., Boatwright, J., 1987. Fractal analysis applied to characteristic segments of the San Andreas Fault. *J. Geophys. Res. Solid Earth* 92, 331–344. <http://dx.doi.org/10.1029/JB092iB01p00331>.
- Ben-Menahem, A., 1991. Four thousand years of seismicity along the Dead Sea Rift. *J. Geophys. Res. Solid Earth* 96, 20195–20216. <http://dx.doi.org/10.1029/91JB01936>.
- Bonilla, M.G., Lienkaemper, J.J., 1990. Visibility of fault strands in exploratory trenches and timing of rupture events. *Geology* 18, 153–156. [http://dx.doi.org/10.1130/0091-7613\(1990\)018<0153:VOFSIE>2.3.CO;2](http://dx.doi.org/10.1130/0091-7613(1990)018<0153:VOFSIE>2.3.CO;2).
- Bøtter-Jensen, L., McKeever, S.W.S., Wintle, A.G., 2003. Optically Stimulated Luminescence Dosimetry. Elsevier, Amsterdam.
- Buylaert, J.P., Murray, A.S., Huot, S., 2008. Optical dating of an Eemian site in Northern Russia using K-feldspar. In: Radiat. Meas. Proceedings of the 15th Solid State Dosimetry (SSD15). 43. pp. 715–720. <http://dx.doi.org/10.1016/j.radmeas.2008.01.027>.
- Buylaert, J.P., Murray, A.S., Thomsen, K.J., Jain, M., 2009. Testing the potential of an elevated temperature IRSL signal from K-feldspar. *Radiat. Meas.* 44, 560–565. <http://dx.doi.org/10.1016/j.radmeas.2009.02.007>.
- Colarossi, D., Duller, G.A.T., Roberts, H.M., Tooth, S., Lyons, R., 2015. Comparison of paired quartz OSL and feldspar post-IR IRSL dose distributions in poorly bleached fluvial sediments from South Africa. *Quat. Geochronol.* 30, 233–238. <http://dx.doi.org/10.1016/j.quageo.2015.02.015>. (LED14 Proceedings).
- Daëron, M., 2005. Rôle, cinématique et comportement sismique à long terme de la faille de Yammouneh, principale branche décrochante du coude transpressif libanais (faille du Levant). Institut de Physique du Globe, Paris.
- Daëron, M., Benedetti, L., Tapponnier, P., Sursock, A., Finkel, R.C., 2004. Constraints on the post ~25-ka slip rate of the Yammouneh fault (Lebanon) using in situ cosmogenic ³⁶Cl dating of offset limestone-clast fans. *Earth Planet. Sci. Lett.* 227, 105–119. <http://dx.doi.org/10.1016/j.epsl.2004.07.014>.
- Daëron, M., Klinger, Y., Tapponnier, P., Elias, A., Jacques, E., Sursock, A., 2005. Sources of the large A.D. 1202 and 1759 Near East earthquakes. *Geology* 33, 529–532. <http://dx.doi.org/10.1130/G21352.1>.
- Daëron, M., Klinger, Y., Tapponnier, P., Elias, A., Jacques, E., Sursock, A., 2007. 12,000-Year-long record of 10 to 13 paleoearthquakes on the Yammouneh Fault, Levant Fault System, Lebanon. *Bull. Seismol. Soc. Am.* 97, 749–771.
- Develle, A.-L., Herreros, J., Vidal, L., Sursock, A., Gasse, F., 2010. Controlling factors on a paleo-lake oxygen isotope record (Yammouneh, Lebanon) since the Last Glacial Maximum. *Quat. Sci. Rev.* 29, 865–886. <http://dx.doi.org/10.1016/j.quascirev.2009.12.005>.
- Develle, A.-L., Gasse, F., Vidal, L., Williamson, D., Demory, F., Van Campo, E., Ghaleb, B., Thouveny, N., 2011. A 250ka sedimentary record from a small karstic lake in the Northern Levant (Yammouneh, Lebanon): Paleoclimatic implications. *Palaeogeogr. Palaeoclimatol. Palaeoecol.* (0031-0182) 305 (1–4), 10–27. <http://dx.doi.org/10.1016/j.palaeo.2011.02.008>.
- Dubertret, L., 1932. Les formes structurales de la Syrie et de la Palestine; leur origine. *CR Acad. Sci.* 195, 65–66.
- Duller, G.A.T., 2003. Distinguishing quartz and feldspar in single grain luminescence measurements. *Radiat. Meas.* 37, 161–165. [http://dx.doi.org/10.1016/S1350-4487\(02\)00170-1](http://dx.doi.org/10.1016/S1350-4487(02)00170-1).
- Durcan, J.A., King, G.E., Duller, G.A.T., 2015. DRAC: Dose Rate and Age Calculator for trapped charge dating. *Quat. Geochronol.* 28, 54–61. <http://dx.doi.org/10.1016/j.quageo.2015.03.012>.
- Elias, A., Tapponnier, P., Singh, S.C., King, G.C.P., Briaies, A., Daëron, M., Carton, H., Sursock, A., Jacques, E., Jomaa, R., Klinger, Y., 2007. Active thrusting offshore Mount Lebanon: source of the tsunamigenic A.D. 551 Beirut-Tripoli earthquake. *Geology* 35, 755–758. <http://dx.doi.org/10.1130/G23631A.1>.
- Ellenblum, R., Marco, S., Agnon, A., Rockwell, T., Boas, A., 1998. Crusader castle torn apart by earthquake at dawn, 20 May 1202. *Geology* 26, 303–306. [http://dx.doi.org/10.1130/0091-7613\(1998\)026<0303:CCTABE>2.3.CO;2](http://dx.doi.org/10.1130/0091-7613(1998)026<0303:CCTABE>2.3.CO;2).
- Ellenblum, R., Marco, S., Kool, R., Davidovitch, U., Porat, R., Agnon, A., 2015. Archaeological record of earthquake ruptures in Tell Ateret, the Dead Sea Fault. *Tectonics* 34, 2105–2117. <http://dx.doi.org/10.1002/2014TC003815>.

- Ferry, M., Meghraoui, M., Abou Karaki, N., Khalil, L., 2011. Episodic behavior of the Jordan Valley section of the Dead Sea Fault inferred from a 14-ka-long integrated catalog of large earthquakes. *Bull. Seismol. Soc. Am.* 101, 39–67.
- Frechen, M., Schweitzer, U., Zander, A., 1996. Improvements in sample preparation for the fine grain technique. *Ancient TL* 14, 15–17.
- Freund, R., Zak, I., Garfunkel, Z., 1968. Age and rate of the sinistral movement along the Dead Sea Rift. *Nature* 220, 253–255.
- Fuchs, M., Straub, J., Zöller, L., 2005. Residual luminescence signals of recent river flood sediments: a comparison between quartz and feldspar of fine- and coarse-grain sediments. *Ancient TL* 23.
- Fuchs, M.C., Kreutzer, S., Burrow, C., Dietze, M., Fischer, M., Schmidt, C., Fuchs, M., 2015. Data processing in luminescence dating analysis: an exemplary workflow using the R package “Luminescence”. In: *Quat. Int.*, 9th New World Luminescence Dating Workshop. 362, pp. 8–13. <http://dx.doi.org/10.1016/j.quaint.2014.06.034>.
- Garfunkel, Z., Zak, I., Freund, R., 1981. Active faulting in the dead sea rift. *Tectonophysics* 80, 1–26. [http://dx.doi.org/10.1016/0040-1951\(81\)90139-6](http://dx.doi.org/10.1016/0040-1951(81)90139-6).
- Gasse, F., Vidal, L., Develle, A.-L., Van Campo, E., 2011. Hydrological variability in the northern levant: A 250 ka multiproxy record from the yammouneh (lebanon) sedimentary sequence. *Clim. Past* 7, 1261.
- Gasse, F., Vidal, L., Van Campo, E., Demory, F., Develle, A.-L., Tachikawa, K., Elias, A., Bard, E., Garcia, M., Sonzogni, C., Thouveny, N., 2015. Hydroclimatic changes in northern Levant over the past 400,000 years. *Quat. Sci. Rev.* 111, 1–8. <http://dx.doi.org/10.1016/j.quascirev.2014.12.019>.
- Galbraith, R.F., Roberts, R.G., Laslett, G.M., Yoshida, H., Olley, J.M., 1999. Optical dating of single and multiple grains of quartz from Jinnium rock shelter, Northern Australia: part I, experimental design and statistical models*. *Archaeometry* 41, 339–364. <http://dx.doi.org/10.1111/j.1475-4754.1999.tb00987.x>.
- Gomez, F., Meghraoui, M., Dalkal, A.N., Hijazi, F., Mouty, M., Suleiman, Y., Sbeinati, R., Darawcheh, R., Al-Ghazzi, R., Barazangi, M., 2003. Holocene faulting and earthquake recurrence along the Serghaya branch of the Dead Sea fault system in Syria and Lebanon. *Geophys. J. Int.* 153, 658–674. <http://dx.doi.org/10.1046/j.1365-246X.2003.01933.x>.
- Goren, L., Castellort, S., Klinger, Y., 2015. Modes and rates of horizontal deformation from rotated river basins: application to the Dead Sea fault system in Lebanon. *Geology* 43, 843–846. <http://dx.doi.org/10.1130/G36841.1>.
- Guérin, G., Mercier, N., Adamiec, G., 2011. Dose-rate conversion factors: update. *Ancient TL* 29, 5–8.
- Guidoboni, E., Bernardini, F., Comastri, A., Boschi, E., 2004. The large earthquake on 29 June 1170 (Syria, Lebanon, and central southern Turkey). *J. Geophys. Res. Solid Earth* 109. <http://dx.doi.org/10.1029/2003JB002523>. (n/a–n/a).
- Huntley, D.J., Baril, M.R., 1997. The K content of the K-feldspars being measured in optical dating or in thermoluminescence dating. *Ancient TL* 15, 11–13.
- Huntley, D.J., Lamothe, M., 2001. Ubiquity of anomalous fading in K-feldspars and the measurement and correction for it in optical dating. *Can. J. Earth Sci.* 38, 1093–1106. <http://dx.doi.org/10.1139/e01-013>.
- Kars, R.H., Wallinga, J., 2009. IRSL dating of K-feldspars: Modelling natural dose response curves to deal with anomalous fading and trap competition. In: *Radiat. Meas., Proceedings of the 12th International Conference on Luminescence and Electron Spin Resonance Dating (LED 2008)*. 44, pp. 594–599. <http://dx.doi.org/10.1016/j.radmeas.2009.03.032>.
- Kars, R.H., Reimann, T., Ankjærgaard, C., Wallinga, J., 2014. Bleaching of the post-IR IRSL signal: new insights for feldspar luminescence dating. *Boreas* 43, 780–791. <http://dx.doi.org/10.1111/bor.12082>.
- King, G.C.P., Nabelek, J., 1985. Role of fault bends in the initiation and termination of earthquake rupture. *Science* 228, 984–987. <http://dx.doi.org/10.1126/science.228.4702.984>.
- Klinger, Y., 2010. Relation between continental strike-slip earthquake segmentation and thickness of the crust. *J. Geophys. Res. Solid Earth* 115. <http://dx.doi.org/10.1029/2009JB006550>. (n/a–n/a).
- Klinger, Y., Le Béon, M., Al-Qaryouti, M., 2015. 5000 yr of paleoseismicity along the southern Dead Sea fault. *Geophys. J. Int.* 202, 313–327. <http://dx.doi.org/10.1093/gji/ggv134>.
- Lamothe, M., Auclair, M., Hamzaoui, C., Huot, S., 2003. Towards a prediction of long-term anomalous fading of feldspar IRSL. In: *Radiat. Meas., Proceedings of the 10th international Conference on Luminescence and Electron-Spin Resonance Dating (LED 2002)*. 37, pp. 493–498. [http://dx.doi.org/10.1016/S1350-4487\(03\)00016-7](http://dx.doi.org/10.1016/S1350-4487(03)00016-7).
- Le Béon, M., Klinger, Y., Mériaux, A.-S., Al-Qaryouti, M., Finkel, R.C., Mayyas, O., Tapponnier, P., 2012. Quaternary morphotectonic mapping of the Wadi Araba and implications for the tectonic activity of the southern Dead Sea fault. *Tectonics* 31. <http://dx.doi.org/10.1029/2012TC003112>. (n/a–n/a).
- Lefevre, M., Klinger, Y., Al-Qaryouti, M., Le Béon, M., Moumani, K., 2018. Slip deficit and time clustering along the Dead Sea fault from paleoseismological investigations. *Sci. Rep.* 8 (1), 4511. <http://dx.doi.org/10.1038/s41598-018-22627-9>. (n.d.).
- Lisiecki, L.E., Raymo, M.E., 2005. A Pliocene-Pleistocene stack of 57 globally distributed benthic $\delta^{18}O$ records. *Paleoceanography* 20, PA1003. <http://dx.doi.org/10.1029/2004PA001071>.
- Liu-Zeng, J., Klinger, Y., Xu, X., Lasserre, C., Chen, G., Chen, W., Tapponnier, P., Zhang, B., 2007. Millennial recurrence of large earthquakes on the Haiyuan fault near Songshan, Gansu Province, China. *Bull. Seismol. Soc. Am.* 97, 14–34.
- Liu-Zeng, J., Shao, Y., Klinger, Y., Xie, K., Yuan, D., Lei, Z., 2015. Variability in magnitude of paleoearthquakes revealed by trenching and historical records, along the Haiyuan fault, China. *J. Geophys. Res. Solid Earth* 120, 8304–8333.
- Marco, S., Stein, M., Agnon, A., Ron, H., 1996. Long-term earthquake clustering: a 50,000-year paleoseismic record in the Dead Sea Graben. *J. Geophys. Res. Solid Earth* 101, 6179–6191. <http://dx.doi.org/10.1029/95JB01587>.
- McCalpin, J.P., 2009. *Paleoseismology*. Academic press.
- Meghraoui, M., Gomez, F., Sbeinati, R., Van der Woerd, J., Mouty, M., Dalkal, A.N., Radwan, Y., Layyous, I., Al Najjar, H., Darawcheh, R., Hijazi, F., Al-Ghazzi, R., Barazangi, M., 2003. Evidence for 830 years of seismic quiescence from palaeoseismology, archaeoseismology and historical seismicity along the Dead Sea fault in Syria. *Earth Planet. Sci. Lett.* 210, 35–52. [http://dx.doi.org/10.1016/S0012-821X\(03\)00144-4](http://dx.doi.org/10.1016/S0012-821X(03)00144-4).
- Messerli, B., 1966. Das Problem der eiszeitlichen Vergletscherung am Libanon und Hermon. *Zeitschrift für Geomorphologie* 10, 37–68.
- Moulin, A., Benedetti, L., Van der Woerd, J., Elias, A., Blard, P., Finkel, R., Braucher, R., Lavé, J., Bourles, D., Daeron, M., et al., 2011. LGM glaciers on Mount Lebanon? New insights from 36Cl exposure dating of moraine boulders. In: *Geophysical Research Abstracts*.
- Murray, A.S., Wintle, A.G., 2000. Luminescence dating of quartz using an improved single-aliquot regenerative-dose protocol. *Radiat. Meas.* 32, 57–73. [http://dx.doi.org/10.1016/S1350-4487\(99\)00253-X](http://dx.doi.org/10.1016/S1350-4487(99)00253-X).
- Nemer, T., Meghraoui, M., 2006. Evidence of coseismic ruptures along the Roum fault (Lebanon): a possible source for the AD 1837 earthquake. *J. Struct. Geol.* 28, 1483–1495. <http://dx.doi.org/10.1016/j.jsg.2006.03.038>.
- Ojala, A.E.K., Francus, P., Zolitschka, B., Besonen, M., Lamoureux, S.F., 2012. Characteristics of sedimentary varve chronologies – a review. *Quat. Sci. Rev.* 43, 45–60. <http://dx.doi.org/10.1016/j.quascirev.2012.04.006>.
- Okubo, P.G., Aki, K., 1987. Fractal geometry in the San Andreas Fault System. *J. Geophys. Res. Solid Earth* 92, 345–355. <http://dx.doi.org/10.1029/JB092iB01p00345>.
- Poirier, J.P., Taher, M.A., 1980. Historical seismicity in the near and Middle East, North Africa, and Spain from Arabic documents (VIIth–XVIIIth century). *Bull. Seismol. Soc. Am.* 70, 2185–2201.
- Prescott, J.R., Hutton, J.T., 1994. Cosmic ray contributions to dose rates for luminescence and ESR dating: large depths and long-term time variations. *Radiat. Meas.* 23, 497–500. [http://dx.doi.org/10.1016/1350-4487\(94\)90086-8](http://dx.doi.org/10.1016/1350-4487(94)90086-8).
- Quennell, A.M., 1959. *Tectonics of the Dead Sea rift*. In: *Proceedings of the 20th International Geological Congress, Mexico*, pp. 385–403.
- Reading, H.G., 1996. *Sedimentary Environments: Processes, Facies and Stratigraphy*, 3rd ed. Blackwell Sci, Oxf.
- Rees-Jones, J., 1995. Optical dating of young sediments using fine-grain quartz. *Ancient TL* 13.
- Reimann, T., Tsukamoto, S., Harff, J., Osadczuk, K., Frechen, M., 2011. Reconstruction of Holocene coastal foredune progradation using luminescence dating — an example from the Świna barrier (southern Baltic Sea, NW Poland). *Geomorphology* 132, 1–16. <http://dx.doi.org/10.1016/j.geomorph.2011.04.017>.
- Rhodes, E.J., 2011. Optically stimulated luminescence dating of sediments over the past 200,000 years. *Annu. Rev. Earth Planet. Sci.* 39, 461–488. <http://dx.doi.org/10.1146/annurev-earth-040610-133425>.
- Roberts, H.M., 2006. Optical dating of coarse-silt sized quartz from loess: Evaluation of equivalent dose determinations and SAR procedural checks. In: *Radiat. Meas., Proceedings of the 11th International Conference on Luminescence and Electron-spin Resonance Dating (LED 2005)*. 41, pp. 923–929. <http://dx.doi.org/10.1016/j.radmeas.2006.05.021>.
- Roberts, H.M., 2008. The development and application of luminescence dating to loess deposits: a perspective on the past, present and future. *Boreas* 37, 483–507. <http://dx.doi.org/10.1111/j.1502-3885.2008.00057.x>.
- Scholz, C.H., 2002. *The Mechanics of Earthquakes and Faulting*. Cambridge University Press.
- Sieh, K.E., 1978. Prehistoric large earthquakes produced by slip on the San Andreas Fault at Palmett Creek, California. *J. Geophys. Res. Solid Earth* 83, 3907–3939. <http://dx.doi.org/10.1029/JB083iB08p03907>.
- Streig, A.R., Dawson, T.E., Weldon, R.J., 2014. Paleoseismic Evidence of the 1890 and 1838 Earthquakes on the Santa Cruz Mountains Section of the San Andreas Fault, Near Corralitos, California. 104, pp. 285–300. <http://dx.doi.org/10.1785/0120130009>.
- Thomsen, K.J., Murray, A.S., Jain, M., Bøtter-Jensen, L., 2008. Laboratory fading rates of various luminescence signals from feldspar-rich sediment extracts. *Radiat. Meas.* 43, 1474–1486. <http://dx.doi.org/10.1016/j.radmeas.2008.06.002>.
- Wechsler, N., Rockwell, T., Klinger, Y., Štěpánčíková, P., Kanari, M., Marco, S., Agnon, A., 2014. A paleoseismic record of earthquakes for the Dead Sea Transform fault between the first and seventh centuries C.E.: nonperiodic behavior of a plate boundary fault. *Bull. Seismol. Soc. Am.* 104, 1329–1347. <http://dx.doi.org/10.1785/0120130304>.
- Wechsler, N., Rockwell, T.K., Klinger, Y., 2018. Variable slip-rate and slip-per-event on a plate boundary fault: the Dead Sea fault in northern Israel. *Tectonophysics* 722, 210–226. <http://dx.doi.org/10.1016/j.tecto.2017.10.017>.
- Wesnousky, S.G., 2006. Predicting the endpoints of earthquake ruptures. *Nature* 444, 358–360. <http://dx.doi.org/10.1038/nature05275>.
- Wallinga, J., Bos, A.J.J., Dorenbos, P., Murray, A.S., Schokker, J., 2007. A test case for anomalous fading correction in IRSL dating. *Quat. Geochronol.* 2, 216–221. <http://dx.doi.org/10.1016/j.quageo.2006.05.014>. (LED 2005).
- Wintle, A.G., 2008. Luminescence dating: where it has been and where it is going. *Boreas* 37, 471–482. <http://dx.doi.org/10.1111/j.1502-3885.2008.00059.x>.
- Wintle, A.G., Murray, A.S., 2006. A review of quartz optically stimulated luminescence characteristics and their relevance in single-aliquot regeneration dating protocols. *Radiat. Meas.* 41, 369–391. <http://dx.doi.org/10.1016/j.radmeas.2005.11.001>.
- Zielke, O., Klinger, Y., Arrowsmith, J.R., 2015. Fault slip and earthquake recurrence along strike-slip faults — contributions of high-resolution geomorphic data. *Tectonophysics* 638, 43–62. <http://dx.doi.org/10.1016/j.tecto.2014.11.004>.
- Zolitschka, B., Francus, P., Ojala, A.E.K., Schimmelmänn, A., 2015. Varves in lake sediments – a review. *Quat. Sci. Rev.* 117, 1–41. <http://dx.doi.org/10.1016/j.quascirev.2015.03.019>.